

Article

Operational Performance and Energy Efficiency of MEX 3D Printing with Polyamide 6 (PA6): Multi-Objective Optimization of Seven Control Settings Supported by L27 Robust Design

Constantine David ¹, Dimitrios Sagris ¹, Markos Petousis ², Nektarios K. Nasikas ³, Amalia Moutsopoulou ², Evangelos Sfakiotakis ², Nikolaos Mountakis ², Chrysa Charou ² and Nektarios Vidakis ^{2,*}

¹ Department of Mechanical Engineering, Serres Campus, International Hellenic University, 62124 Serres, Greece; david@ihu.gr (C.D.); dsagris@ihu.gr (D.S.)

² Department of Mechanical Engineering, Hellenic Mediterranean University, 71410 Heraklion, Greece; markospetousis@hmu.gr (M.P.); amalia@hmu.gr (A.M.); esfakiotakis@hmu.gr (E.S.); mountakis@hmu.gr (N.M.); charou@hmu.gr (C.C.)

³ Division of Mathematics and Engineering Sciences, Department of Military Sciences, Hellenic Army Academy, 16673 Vari, Greece; nasikas@sse.gr

* Correspondence: vidakis@hmu.gr; Tel.: +30-2810379227

Featured Application: The findings presented herein can be directly applied for the prediction and optimization of the compressive strength and the energy consumption of parts to be manufactured with the material extrusion 3D printing process with the Polyamide 6 polymer.

Abstract: Both energy efficiency and robustness are popular demands for 3D-printed components nowadays. These opposing factors require compromises. This study examines the effects of seven general control variables on the energy demands and the compressive responses of polyamide (PA6) material extrusion (MEX) 3D printed samples. Nozzle Temperature, Layer Thickness, Orientation Angle, Raster Deposition Angle, Printing Speed, Bed Temperature, and Infill Density were studied. An L27 orthogonal array was compiled with five replicas. A total of 135 trials were conducted, following the ASTM D695-02a specifications. The stopwatch method was used to assess the construction time and energy usage. The compressive strength, toughness, and elasticity modulus were experimentally determined. The Taguchi technique ranks each control parameter's impact on each response measure. The control parameter that had the greatest impact on both energy use and printing time was layer thickness. Additionally, the infill density had the greatest influence on the compressive strength. Quadratic regression model equations were formed for each of the response measures. The ideal compromise between mechanical strength and energy efficiency is now reported, with merit related to technological and economic benefits.

Keywords: polyamide 6 (PA6); material extrusion (MEX); optimization; compressive strength; energy efficiency; energy consumption; robust design; Taguchi analysis



Citation: David, C.; Sagris, D.; Petousis, M.; Nasikas, N.K.; Moutsopoulou, A.; Sfakiotakis, E.; Mountakis, N.; Charou, C.; Vidakis, N. Operational Performance and Energy Efficiency of MEX 3D Printing with Polyamide 6 (PA6): Multi-Objective Optimization of Seven Control Settings Supported by L27 Robust Design. *Appl. Sci.* **2023**, *13*, 8819. <https://doi.org/10.3390/app13158819>

Academic Editor: Fuji Wang

Received: 7 July 2023

Revised: 22 July 2023

Accepted: 28 July 2023

Published: 30 July 2023



Copyright: © 2023 by the authors. Licensee MDPI, Basel, Switzerland. This article is an open access article distributed under the terms and conditions of the Creative Commons Attribution (CC BY) license (<https://creativecommons.org/licenses/by/4.0/>).

1. Introduction

The ability to manufacture intricate geometries [1], the high levels of customization, and other benefits have contributed to the growth of additive manufacturing (AM) technology over the past 25 years [2,3]. One of these benefits is its reduced environmental impact due to the process's reduced material waste [4–6]. To understand this facet of the AM technique and its role in a cyclical economy, as well as the equivalent environmental perceptions, a lot of research has been conducted [2,4,5,7,8]. Among the several methods of AM, Fused Filament Fabrication (FFF) is a material extrusion (MEX) process involving layer-by-layer [9] melting of filament strands through a heated nozzle to create objects using Computer-Aided Design (CAD) data [6,10,11]. The impact of the processing variables, such

as the infill pattern, on the mechanical performance and dimensional precision of items fabricated using the FFF technique has been investigated [12]. The energy used throughout the 3D printing of components is one of the research topics that have an impact on the sustainability of the AM method [2,13]. To establish the ecological effect of AM [14,15], researchers have examined the consumption of energy of the AM procedure [16,17]. It is reported that in the vat photopolymerization (VPP) process, the energy consumption varies from (Specific Energy Consumption—SEC) 21 to 33 KWh/Kg, while in the FFF process, it ranges from 23 to 346 KWh/Kg for the 3D printing of the ABS polymer [14,15]. From this energy, 51.7% is the energy consumed by the motors, 41.4% by the heat elements, and 6.9% by the fans [16], while a model for the prediction of the energy consumption has been proposed [17].

Polymers such as acrylonitrile butadiene styrene (ABS) [18], polylactic acid (PLA) [19,20], poly (methyl methacrylate) (PMMA) [21], and polycarbonate (PC) [22], among others, have been investigated for their energy demands during the 3D printing of parts with the MEX method. Adaptive multi-layer customization [23], machine learning methods [24], and statistical modeling tools [25], made for examining and maximizing the influence of the 3D printing settings on the consumption of energy in methods of additive manufacturing [26], have all been used in this context. Modeling tools, such as Neural Networks [27], Analysis of Variances (ANOVA) [28], Taguchi design of experiments [29,30], Box Behnken design [31], have been applied for the analysis of experimental data in 3D printing, related to the effect of the 3D printing settings on the performance of the parts. Additionally, the economic viability and ecological impact of FFF, both have an extensive amount of room for improvement [32].

Numerous studies have been conducted to determine how the 3D printing factors influence the mechanical properties of the final component [26,33,34]. A crucial step in creating 3D geometries is choosing the appropriate infill pattern as well as the printing speed [12,35]. Christiyan et al. [36] examined the impact of printing speed and layer height on composites consisting of ABS with hydrous magnesium silicate using the FFF process. By properly adjusting the process parameters, the mechanical performance of the fabricated objects can be greatly enhanced [37]. The optimization of process parameters has drawn significant interest from numerous researchers. Some of these parameters include the speed of printing [34], the diameter of the nozzle, the raster angle [38], layer thickness [39], and chamber temperature [40], which are often optimized using the Taguchi method [41]. Yao et al. [42] investigated how the mechanical properties of 3D-printed poly-lactic acid (PLA, a thermoplastic material) pieces were affected by the orientation angle of the parts [43]. A constitutive model for 3D printed parts was developed by Somireddy M. et al. [44], and this model can depict how layer thickness and building orientation affect the way 3D printed items respond based on their materials. The raster orientation's effects on axial loading fatigue life have been studied by Ziemian et al. [45–47]. According to the research, the 45°/45° raster orientation performed the best. As previously stated, FFF 3D printing involves a staggeringly high number of process variables [46–49], and all of them could have an effect on the end part's mechanical characteristics [48]. Several studies have revealed numerous variables that may potentially alter the 3D-printed objects' mechanical properties and fatigue life [50–53]. The mechanical characteristics and dimensional accuracy of the FFF parts are extensively reported [54–56].

Polyamides (polymers with amide bonds connecting the monomeric units), can be sourced from nature, such as proteins, while synthetic polyamides also exist, such as polycaprolactam (Polyamide 6—PA6) and poly(hexamethylene adipamide) (Polyamide 6.6—PA6.6) [57]. Similar to polyesters, polyamides can be divided into three groups based on the main chain's chemical makeup: aliphatic, semi-aromatic, and aromatic polyamides [58]. Among these, polyamide 6 (PA6) has emerged as one of the plastics for engineering with a significant variety of uses due to its reasonable price, strong heat resistance, and good processing qualities [59–62]. As expected, it has been employed in 3D printing applications, and its performance has been investigated and reported [63]. Fur-

thermore, the use of polyamide 6 (PA6) as a practical matrix material in lightweight carbon fiber-reinforced, graphene nanoplatelet-reinforced, or reinforcing fibers of cement mortars is increasing [64–68]. Its mechanical performance under tensile and fatigue loadings in 3D printing has been thoroughly studied [68–75]. S. Terekhina et al. [48] performed a fatigue investigation focused on the viscoelastic response of PA6 in FFF 3D printing. Flexural tests were conducted, and the porosity and surface roughness were also assessed. The sustainability of polyamides in 3D printing has also been investigated through their ability to be reused after multiple thermomechanical processes during their recycling process [76].

Research in polyamides in FFF extends also to the process parameters' effect on composites having polyamides as the matrix material. Ceramics, such as Titanium Nitride (TiN), Copper (Cu), and Cuprous Oxide (Cu₂O), have been introduced to polyamide matrices [77,78], as has Zirconium Dioxide (ZrO₂) [79]. In this direction, Benfriha K. et al. [59] have investigated PA6/Carbon fiber composites. The outcome of the research supported the impact of these variables on the bonding formation during the FFF method and the mechanical responses of the printed items. In addition, Zhongbei Li et al. [80] investigated the effects of eight FFF parameters on the characteristics of PA6/PA66 composite samples using the Taguchi technique. Based on the results of their study, it was found that samples with infill patterns with a zigzag configuration and a layer thickness of 0.15 mm showed greater surface quality, dimensional accuracy, and mechanical performance.

The compressive strength of FFF items has, however, received scant attention in the literature [19]. Even though compression loading is a relatively typical loading type, in-depth research on material reactions to compression loads is rarely the focus of research [81]. Furthermore, no study has yet shown the power requirements for 3D printed PA6 polymer components or how the 3D printing settings employed for the particular polymer influence the amount of energy needed to build the parts, despite the PA6 polymer's outstanding performance for sustainable applications.

In this study, Polyamide 6 was used as the material to examine the impact of seven general control factors as well as the energy and mechanical response during the compressive response of MEX 3D printed samples. These factors are Orientation Angle (ORA), Raster Deposition Angle (RDA), Nozzle Temperature (NT), Bed Temperature (BT), Infill Density (ID), Layer Thickness (LT), and Printing Speed (PS). PA6 was purchased in the form of pellets, and it was made into filament using the extrusion process. The samples were produced utilizing various 3D printing setting combinations. The 3D printed specimens were subjected to experimental testing to ascertain their mechanical properties under compression stress, in accordance with the international standard ASTM D695-02a for testing polymers under compressive loading. The stopwatch method was used to keep track of the amount of time. The energy required during the 3D printing process was monitored with the respective equipment. A detailed analysis of the fracture behavior and morphological characteristics was performed. An L27 orthogonal array was constructed using the Taguchi method to process the experimental data, and Quadratic Regression Modeling (QRM) was then used to develop equations for the predictions of the various response factors explored in the research. To our knowledge, no other study examines as many variables simultaneously for MEX 3D printed PA6 parts' energy usage and mechanical performance, especially in compressive loading. The modeling techniques employed demonstrated the requirement for such an analysis, as they revealed that the parameters under study have varying effects on the work's response characteristics.

While the orientation angle and the infill density had a substantial impact on the components' compressive strength, on the other hand, printing speed and layer thickness had a considerable impact on energy usage. A cause-and-effect has been prepared showing the parameters affecting the compressive strength and the energy consumption and is presented in the Supplementary material of the study (Figure S1). The given prediction models have had their dependability confirmed and are suitable for immediate application in industrial applications. The authors specifically decided to examine and conduct tests

on compressive specimens despite their lengthy printing times, large volumes, and weight (as opposed to tensile specimens):

- Existing research lacks extensive data, particularly when it comes to multi-parametric tests. Due to the high cost of 3D printing, and the need for a more robust compression test apparatus, there is a shortage of such scientific findings. Given that compressive mechanical stress occurs frequently over the operational life of 3D-printed working components, the paucity of compression test results documentation is evident [82].
- The compressive samples' increased volume enabled the monitoring and documentation of their weight, printing time, and power consumption and resulted in measures that are accurate and trustworthy.

The current study provides a thorough and in-depth assessment of the general process parameter optimization for Polyamide 6 (PA6), one of the most widely used polymers in 3D printing. With the help of the related predictive equations, the environmental, economic, and mechanical behavior outcomes of 3D-printed PA6 samples are thus at hand.

2. Materials and Methods

The methodology used in the present investigation is depicted in Figure 1. More particularly, Figure 1a illustrates the stages of the method used for the specimens' preparation, assessment, and characterization, as well as the evaluation of the experimental results of the present study. Pictures from the trial-based course are shown in Figure 1b. In particular, Figure 1b shows: how the raw material was dried (PA6 Novamid N X 160 pellets acquired from DSM Engineering Materials at 60 °C for 24 h) in subfigure no 1, the extrusion of filament using a 3devo precision single screw extruder from the Netherlands' Utrecht (filament's diameter 1.75 mm, first and fourth heat zones: 190 °C, second and third heat zones: 220 °C, 3.50 rpm, fan: 80.0%) in subfigure no 2, the drying process of the created filament (4 h at 60 °C) in subfigure no 3, and 3D printing of the samples in agreement with ASTM D695-02a standard (five replicas for each set of 3D printing settings, using an Intamsys 3D Printer, Funmat HT, from Shanghai, China) in subfigure no 4. The 3D printing procedure's parameters are displayed in Figure 2. The energy assessments conducted during the 3D printing procedure employing a digital multimeter Rigol DM-3058E (RIGOL Technologies, Shanghai, China) are presented in subfigure no 5 of Figure 1, the examination of the specimens' morphology using an optical microscope (Kern OKO-1, Germany; 5-MP type with ODC-832 camera) in subfigure no 6 of Figure 1, and the evaluation of the specimens' compressive strength (Instron KN-1200 universal testing machine, from Norwood, Massachusetts, USA) in subfigure no 7 of Figure 1. The robust design algorithm implemented in this study for the optimization and evaluation of the experimental findings is shown in Figure 1c.

Thermogravimetric Analysis (TGA) (Perkin Elmer Diamond, 30–550 °C heating course with a 10 °C/min step) and Differential Scanning Calorimetry (DSC) (TA Instruments DSC 25 apparatus, 25–220—25 °C heating cycle, 15 °C/min step) were used to assess the specific PA6 material's thermal sensitivity, and the relevant graphs are shown in Figure 2a,b, correspondingly. This investigation aimed to examine the thermal sensitivity of the particular PA6 material to make sure that the temperatures utilized to produce filament through melt-extrusion and the extrusion process in the 3D printer do not affect the thermal stability of the material or result in material degradation. The TGA measurements (Figure 2a) show that the Bed Temperature (BT) and the Nozzle Temperature (NT) used in the study for the 3D printing of the samples are lower than the temperature at which the PA6 starts to degrade. So, no such phenomena are expected to affect the performance of the 3D-printed samples. Additionally, the DSC curve (Figure 2b) shows that the temperatures used are in a range where the PA6 is not changing phase.

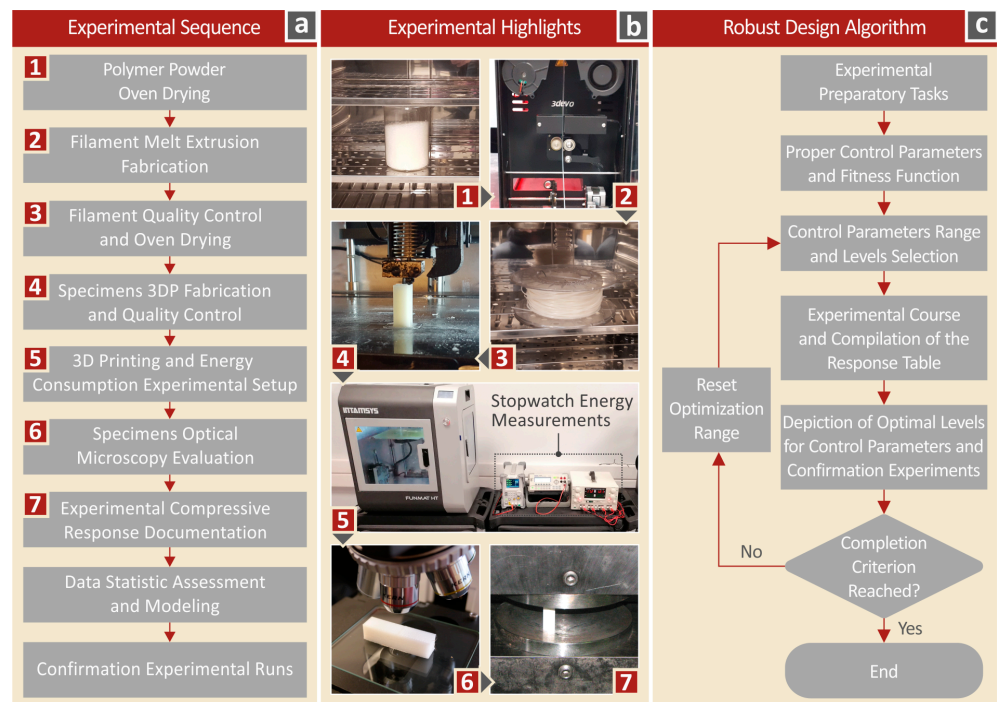


Figure 1. Work procedure: (a) methodology steps of the experiments; (b) experimental procedure highlights; (c) robust design algorithm.

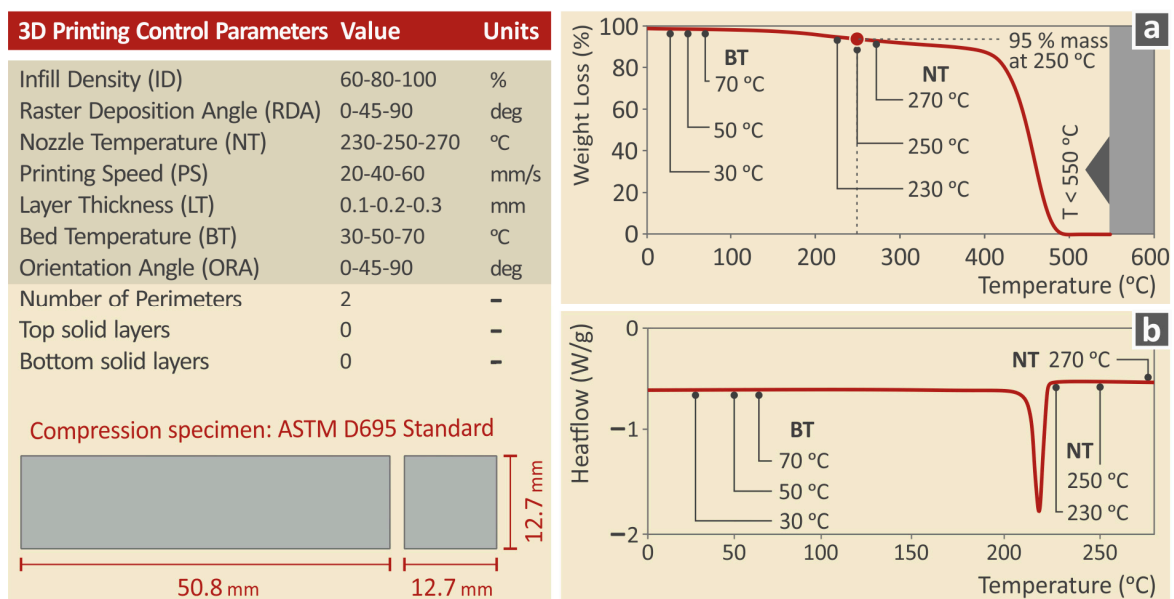


Figure 2. Values for 3D printing parameters and the compression test sample’s geometry made in accordance with ASTM D695 specifications are shown. The right side of the figure shows (a) a TGA graph of the weight loss versus temperature for the particular PA6 utilized in the study and (b) a DSC graph.

The three primary components of the overall electric energy consumption during the MEX-AM course are (i) consumption at machine startup, (ii) consumption throughout the manufacturing 3D printing stage, and (iii) consumption after the manufacturing process, until the machine shutdown. The following equations are used to calculate total energy consumption [18]:

$$E_{total} = E_{thermal} + E_{motion} + E_{auxiliary} \tag{1}$$

where:

$$E_{thermal} = E_{heating} + E_{cooling} \quad (2)$$

E_{motion} is the amount of the 3D printer's motors power consumption, and

$$E_{auxiliary} = E_{startup} + E_{steadystate} + E_{shutdown} \quad (3)$$

Is the power used by the 3D printer's remaining components and electrical circuits.

The Specific Printing Energy (SPE) measure is produced by the subsequent equation, and it is a ratio showing the required energy per gram of material manufactured:

$$SPE = \frac{EPC}{w} [\text{MJ/g}] \quad (4)$$

As opposed to the Specific Printing Power Metric (SPP), which is derived from the subsequent equation, and additionally, to the SPE metric, it also considers the required time (power per gram):

$$SPP = \frac{EPC}{PT \cdot w} \cdot 10^3 [\text{kW/g}] \quad (5)$$

where the three variables w , PT , and EPC stand for the real weight for each sample, the actual printing time for every test run, and the total energy used by the 3D printer.

2.1. Compression Experiments

Compression experiments were conducted on an Instron KN1200 universal testing machine (Figure 3b) to evaluate the behavior of the PA6 3D printed samples when exposed to compressive loads. A compression speed of 1.30 mm/min was selected for the test in agreement with ASTM D695 specifications. The specimens are mounted between the two plates of the testing machine, whereas the compression load is applied in the longitudinal direction.

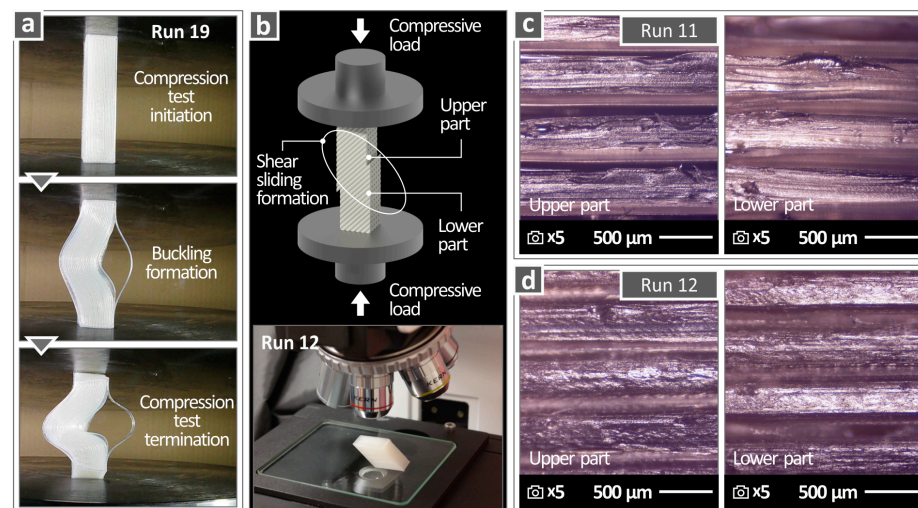


Figure 3. (a) A 3D printed specimen's compression test stages up to delamination failure due to buckling (Runs 19), (b) graphical representation and microscopic examination of the fractured surface, (c,d) Micrographs of two corresponding samples' upper- and lower-fractured surfaces (Run 11, 12) that failed by shear sliding.

2.2. Methodology for the Analysis of Variance (ANOVA) and Experimental Design

A robust design methodology was used in this work for the design of the experiment phase of the current research, specifically the Taguchi method as defined by Phadke [83]. The Taguchi method is a statistical method for the determination of the optimum parameters that lead to improved product quality, while at the same time, this is achieved with a

reduced number of the required experimental repetitions [83–85]. Seven 3D printing characteristics that are present and constant across all MEX 3D printing systems were chosen as the control factors. The control settings, including Raster Deposition Angle (RDA, deg), Orientation Angle (ORA, deg), Bed Temperature (BT, °C), Layer Thickness (LT, mm), Infill Density (ID, %), Nozzle Temperature (NT, °C), and Printing Speed (PS, mm/min), were chosen after carefully examining the available research [86] on PA6 material used in MEX 3D printing and considering industry standards. The same references and current body of knowledge on the subject were used to define the range of values for these factors.

An L27-array (135 separate tests for the overall modeling technique, five replicas per run) was developed using the Taguchi design of experiments for the formulation of the investigational procedure and the assessment of test findings. To implement an identical full factorial modeling method, 5×3^7 distinct tests would be required, which is not possible to implement within a research study.

This study investigated how the chosen control settings affected two different sets of response metrics. The printing period (in seconds), the weight of the specimen (in grams), energy per piece (EPC, in megajoules), specific energy consumption (SPE, in megajoules per gram), and specific power consumption (SPP, in kilowatts per gram) made up the initial set of response parameters that were related to energy. The second set was composed of compression strength-related response settings, including compressive toughness (in megajoules per cubic meter), compressive toughness (in megapascals), and compressive strength (in megapascals). An analysis of variance (ANOVA) was carried out. The analysis provided metrics related to the reliability of the process (R values) for each response parameter studied. Additionally, prediction models for the response parameters were formed, i.e., equations for the calculation of each response parameter as a function of the control parameter studies (the second to last block of Figure 1a refers to this step of the process; the block also refers to the Taguchi method for the statical analysis of the experimental data, which preceded the ANOVA). To verify the effectiveness of these prediction models, two additional confirmation experimental runs were carried out, and the experimental findings were correlated with the calculated ones from the prediction models (Figure 1a, last block). The seven parameters of control (3D printing factors) and their respective levels are shown in Table 1, as they were created and researched in the course of the study.

Table 1. Design of the Taguchi L27: Control Factors and Levels.

Run	ORA	RDA	LT	ID	PS	NT	BT
1	0.0	0.0	0.1	60.0	20.0	230	30.0
2	0.0	0.0	0.1	60.0	40.0	250	50.0
3	0.0	0.0	0.1	60.0	60.0	270	70.0
4	0.0	45.0	0.2	80.0	20.0	230	30.0
5	0.0	45.0	0.2	80.0	40.0	250	50.0
6	0.0	45.0	0.2	80.0	60.0	270	70.0
7	0.0	90.0	0.3	100.0	20.0	230	30.0
8	0.0	90.0	0.3	100.0	40.0	250	50.0
9	0.0	90.0	0.3	100.0	60.0	270	70.0
10	45.0	0.0	0.2	100.0	20.0	250	70.0
11	45.0	0.0	0.2	100.0	40.0	270	30.0
12	45.0	0.0	0.2	100.0	60.0	230	50.0
13	45.0	45.0	0.3	60.0	20.0	250	70.0
14	45.0	45.0	0.3	60.0	40.0	270	30.0
15	45.0	45.0	0.3	60.0	60.0	230	50.0
16	45.0	90.0	0.1	80.0	20.0	250	70.0
17	45.0	90.0	0.1	80.0	40.0	270	30.0
18	45.0	90.0	0.1	80.0	60.0	230	50.0

Table 1. Cont.

Run	ORA	RDA	LT	ID	PS	NT	BT
19	90.0	0.0	0.3	80.0	20.0	270	50.0
20	90.0	0.0	0.3	80.0	40.0	230	70.0
21	90.0	0.0	0.3	80.0	60.0	250	30.0
22	90.0	45.0	0.1	100.0	20.0	270	50.0
23	90.0	45.0	0.1	100.0	40.0	230	70.0
24	90.0	45.0	0.1	100.0	60.0	250	30.0
25	90.0	90.0	0.2	60.0	20.0	270	50.0
26	90.0	90.0	0.2	60.0	40.0	230	70.0
27	90.0	90.0	0.2	60.0	60.0	250	30.0

3. Results

3.1. Evaluation of Compressive Failure Modes and Morphological Traits

Figure 4 shows microscopic images that were captured from the top surface of specimens that were fabricated using various control parameter settings. Since each specimen was 3D printed using different 3D printing settings, the distinction between the created structures is clear. Every image displays the texture of the 3D-printed specimen from the run mentioned in the image. As shown, excellent layer fusion is presented in the images, with layers having a uniform shape and no defects or voids visible. This indicates that the settings were appropriate for the PA6 specimens' 3D printing with the MEX method. For a presentation of one microscopic image from each one of the 27 experimental runs, please see the paper's Supplementary material (Figure S2).

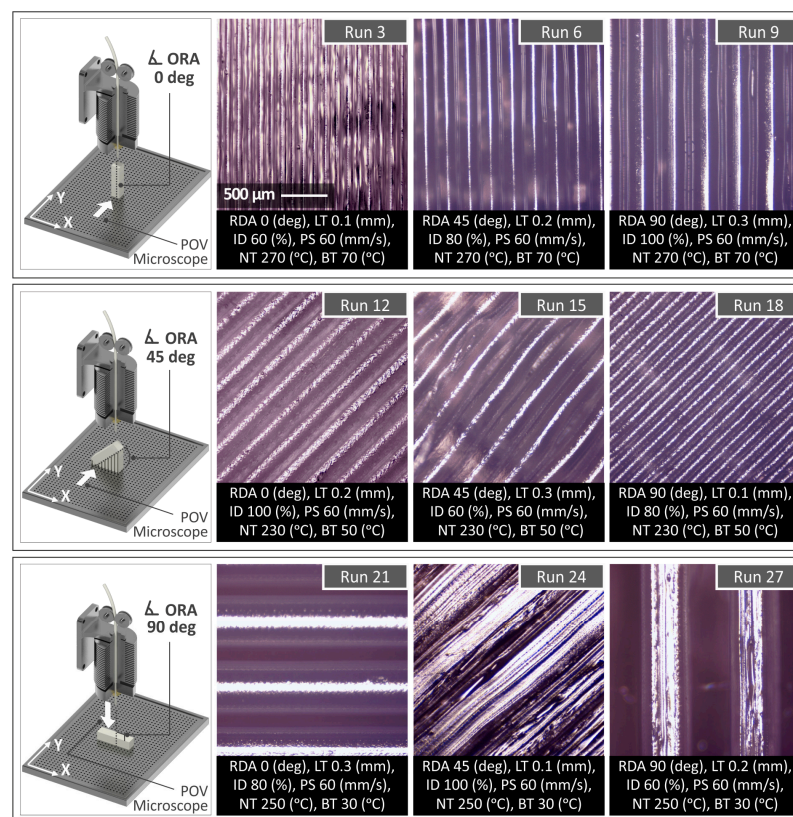


Figure 4. Microscopic images of specimens created using several 3D printing parameters. The specimen's 3D printing raster deposition angle is displayed in every case. On the graphic on the left side, the white arrow indicates the surface of the sample that was captured and presented in the microscope images on the right side.

The samples that underwent a compression test in accordance with ASTM D695 are shown in Figure 5. Depending on the results of the compression experiments, a categorization of the compressive failure types can be determined. The resulting compressive modes of failure due to these tests can be classified into three primary failure categories that are each split into subcategories. The main categories are flexural buckling, kinking, and shear failures. The first and most common type is flexural buckling failure, which involves three distinct sub-modes: lateral buckling (runs 4, 5, 6, 9, 16, 17, 18); interlaminar delamination causes buckling (runs 19, 20, 21, 22), interfacial debonding and buckling (runs 7, 8, 25, 26, 27); and buckling associated with twisting around the longitudinal axis (runs 11, 13, 24). The kinking failure is the second one, either with a single (run 10) or double (runs 1, 2, 3, 14, 15) kink, and the third failure mode is shearing failure with sliding (runs 12, 23).

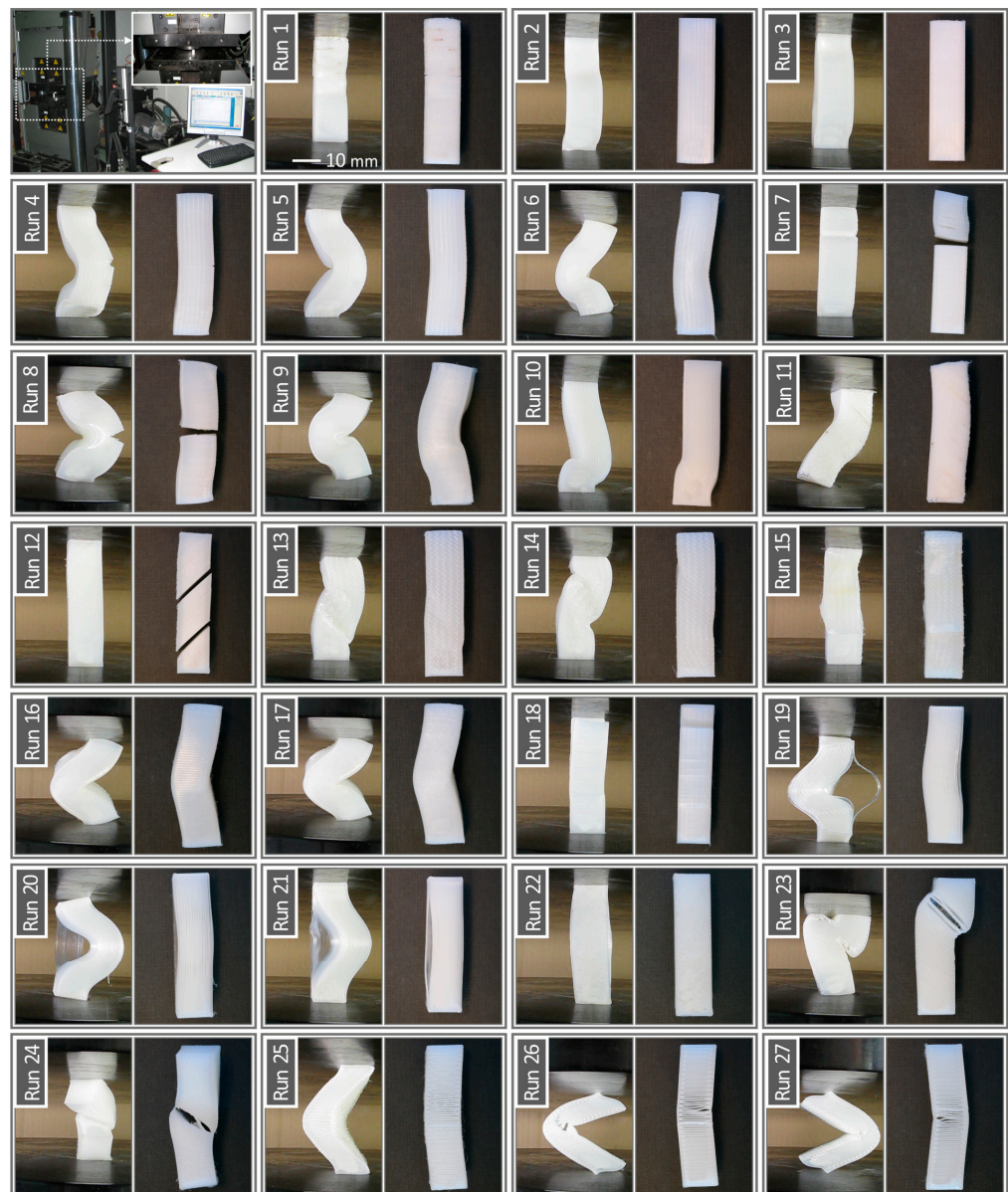


Figure 5. Specimen failure during compression testing.

The factors in the 3D printing process are related to each distinct failure mode. The infill density (ID), in conjunction with the printing orientation angle (ORA), are the primary factors that influence the failure mechanism of the samples. Changes in the values of these factors affect the failure mechanism in the samples, as explained below. The samples (runs

1 to 9) show the flexural failure of buckling or kinking mode at a printing angle of 0° , demonstrating maximal compressive strength, which even grows in proportion to the infill density (ID), in contrast to other printing angle values. The combination of ORA and RDA control settings that results in specimens with 45-degree-inclined layers causes shear failure because, in the case of low nozzle temperature (runs 11, 12), insufficient interlayer bonding causes sliding at the 45-degree shear plane.

For specimens with a 90° printing angle, flexural buckling failure is observed, either with interlaminar delamination (samples 19, 20, and 21) for a 0° RDA or with debonding at the interfaces of adjacent layers for a 90° RDA. As a result, the RDA contributes by altering the primary failure mechanism, which causes secondary failure modes. For a 45° RDA, for instance, the specimen experiences a twist-type shearing failure concerning the longitudinal axis. Additionally, a specimen that experiences laminar failure is typically strengthened by a 45° RDA angle because it prevents layer separation brought on by significant interlaminar pressures operating at the boundary of two adjacent layers. Finally, the experimental findings exposed a straightforward correlation between the infill density and the 3D-printed samples' highest compressive resistance.

The highest compressive load that the specimen can withstand during the compression test is known as the ultimate compressive strength. This indicates that the distortion caused by the maximum compression load signifies the beginning of the material rupture. No matter the particular failure mode that might take place, the sample's infill density maintains its consistent compressive strength [19].

The process for examining the failure of the 3D-printed PA6 samples brought on by compressive force is demonstrated in Figure 3. The specific failure mechanism in question in this case is buckling. The examined sample is precisely positioned, with its longitudinal axis aligned with the plunger's center line and its ends parallel to the compression plates between them. The compression load is then applied by moving the plunger axially at the 1.3 mm/min standard testing speed. After being subjected to compressive stress, the specimen gradually buckles and is deformed into the C-shape because of the specimen contact friction, the square shape of the specimen end surface, and the support conditions that result. According to the 3D printed structure, buckling failure occurs when the elastic critical compressive load is exceeded. The buckling happens on the plane where the sample has the lower second moment of area value. The samples were exposed to compressive loading until they entirely failed. An optical microscope is used to study the fractured surfaces in order to comprehend the failure mechanism. The markings on the PA6 strands caused by shear sliding, which originated due to the compressive loading, are visible in the micrographs of two example sample failures (runs 11 and 12).

3.2. Experimental Results and Taguchi Design

For Compressive Strength (MPa), Toughness (MJ/m^3), Modulus of Elasticity (MPa), and Weight (g) response settings, Table 2 shows, for each individual run, the average values and standard deviations. The response components related to energy, alongside their average values and standard deviations (Printing Time, SPE, EPC, and SPP), are shown in Table 3 (the deviation presented is the calculated one from the experimental results. It refers only to the specific data, so there is no coverage factor). Please consult the Supplementary file for more information about the experimental findings from the completed experiments that are presented (Tables S1 and S2). It should be noted that the average values of the printing time were calculated from the values of the measured printing time for each repetition of each run. The average values come from the five measurements in each run for the printing time. These values are presented analytically in Table S2 of the supplementary material of the study. The printing time measurements were integer numbers without decimal parts since there was no point in measuring the fragment of the seconds. Therefore, it is not strange that most of the average values are also integer numbers. As expected, this is not the case for their deviation.

Table 2. Weight, Compressive Strength (sB), Compressive Modulus of Elasticity (E), and Compressive Toughness Means and Standard Deviations of Evaluated Responses.

Run	Weight (g)	sB (MPa)	E (MPa)	Toughness (MJ/m ³)
1	5.62 ± 0.15	11.66 ± 1.92	224.78 ± 25.77	1.30 ± 0.17
2	5.49 ± 0.11	14.42 ± 0.81	224.41 ± 4.44	1.68 ± 0.12
3	5.53 ± 0.07	18.19 ± 0.81	258.81 ± 12.40	2.17 ± 0.09
4	6.74 ± 0.18	13.63 ± 0.66	249.80 ± 7.99	1.40 ± 0.10
5	6.35 ± 0.13	21.82 ± 2.43	300.78 ± 29.62	2.55 ± 0.40
6	6.38 ± 0.17	24.12 ± 1.62	243.90 ± 11.32	3.15 ± 0.24
7	6.64 ± 0.29	26.73 ± 3.92	286.52 ± 27.15	2.80 ± 0.53
8	8.41 ± 0.41	31.76 ± 4.32	318.56 ± 38.38	3.91 ± 1.01
9	8.36 ± 0.11	30.31 ± 1.19	261.54 ± 10.04	3.86 ± 0.07
10	8.15 ± 0.12	31.50 ± 1.52	281.00 ± 27.99	4.08 ± 0.23
11	6.40 ± 0.08	34.49 ± 0.36	290.70 ± 20.54	4.54 ± 0.16
12	8.00 ± 0.12	22.81 ± 2.36	229.48 ± 24.95	3.14 ± 0.33
13	5.53 ± 0.04	9.99 ± 0.72	66.49 ± 9.12	1.35 ± 0.06
14	5.44 ± 0.13	10.39 ± 0.83	76.96 ± 1.77	1.44 ± 0.07
15	5.72 ± 0.56	3.04 ± 1.91	28.18 ± 13.62	0.33 ± 0.29
16	7.24 ± 0.41	17.20 ± 1.02	128.45 ± 17.33	2.16 ± 0.18
17	7.10 ± 0.13	17.60 ± 0.79	145.80 ± 11.10	2.25 ± 0.13
18	6.84 ± 0.17	12.46 ± 1.97	99.42 ± 15.86	1.64 ± 0.16
19	6.10 ± 0.52	0.57 ± 0.19	52.46 ± 35.37	0.06 ± 0.01
20	6.02 ± 0.12	5.29 ± 4.43	173.53 ± 103.52	0.55 ± 0.36
21	6.19 ± 0.27	1.24 ± 0.52	60.27 ± 39.53	0.16 ± 0.04
22	7.64 ± 0.16	36.99 ± 2.21	321.08 ± 50.55	4.91 ± 0.27
23	7.12 ± 0.16	18.07 ± 4.24	206.92 ± 61.23	2.40 ± 0.58
24	8.18 ± 0.18	26.97 ± 4.27	323.68 ± 32.31	3.40 ± 0.70
25	5.65 ± 0.05	5.91 ± 1.13	66.93 ± 5.70	0.84 ± 0.18
26	5.22 ± 0.06	9.93 ± 1.88	86.75 ± 17.95	1.29 ± 0.23
27	5.52 ± 0.09	11.82 ± 2.11	108.24 ± 19.73	1.62 ± 0.31

Table 3. Printing time (s), EPC (MJ), SPE(MJ/g), and SPP's (kW/g) mean values and standard deviations of measured responses.

Run	Printing Time (s)	EPC (MJ)	SPE (MJ/g)	SPP (kW/g)
1	8755.00 ± 253.07	0.935 ± 0.039	0.166 ± 0.005	0.019 ± 0.001
2	3965.00 ± 171.75	0.719 ± 0.029	0.131 ± 0.006	0.033 ± 0.002
3	3145.20 ± 156.99	0.713 ± 0.034	0.129 ± 0.007	0.041 ± 0.003
4	3500.00 ± 165.61	0.787 ± 0.052	0.117 ± 0.010	0.033 ± 0.003
5	2620.00 ± 88.87	0.431 ± 0.029	0.068 ± 0.005	0.026 ± 0.002
6	2040.00 ± 89.17	0.467 ± 0.011	0.073 ± 0.001	0.036 ± 0.002
7	3775.00 ± 83.68	0.468 ± 0.028	0.071 ± 0.004	0.019 ± 0.001
8	1950.00 ± 64.68	0.359 ± 0.025	0.043 ± 0.003	0.022 ± 0.002
9	1430.00 ± 45.45	0.361 ± 0.015	0.043 ± 0.002	0.030 ± 0.001
10	7030.00 ± 367.74	1.583 ± 0.071	0.194 ± 0.010	0.028 ± 0.002
11	4615.40 ± 164.19	0.504 ± 0.035	0.079 ± 0.006	0.017 ± 0.001
12	3280.00 ± 211.83	0.576 ± 0.036	0.072 ± 0.004	0.022 ± 0.002
13	4155.00 ± 251.41	0.901 ± 0.059	0.163 ± 0.010	0.039 ± 0.003
14	2380.00 ± 59.30	0.252 ± 0.016	0.046 ± 0.004	0.020 ± 0.002
15	1915.00 ± 74.52	0.323 ± 0.017	0.057 ± 0.004	0.030 ± 0.002
16	10,980.00 ± 540.65	1.804 ± 0.079	0.250 ± 0.020	0.023 ± 0.003
17	7739.80 ± 285.72	1.009 ± 0.046	0.142 ± 0.006	0.018 ± 0.001
18	5970.00 ± 188.00	1.052 ± 0.073	0.154 ± 0.014	0.026 ± 0.002
19	2652.00 ± 135.27	0.396 ± 0.028	0.065 ± 0.005	0.025 ± 0.002
20	1345.00 ± 54.80	0.288 ± 0.022	0.048 ± 0.003	0.036 ± 0.002
21	1020.00 ± 40.79	0.144 ± 0.009	0.023 ± 0.001	0.023 ± 0.000
22	10,030.20 ± 357.64	1.300 ± 0.102	0.170 ± 0.013	0.017 ± 0.002
23	5258.00 ± 195.42	0.972 ± 0.028	0.137 ± 0.007	0.026 ± 0.001
24	3911.20 ± 179.09	0.468 ± 0.033	0.057 ± 0.004	0.015 ± 0.001
25	3360.00 ± 133.82	0.504 ± 0.029	0.089 ± 0.006	0.027 ± 0.001
26	1825.00 ± 85.67	0.360 ± 0.016	0.069 ± 0.003	0.038 ± 0.003
27	1379.80 ± 82.81	0.180 ± 0.006	0.033 ± 0.001	0.024 ± 0.002

Box plots are created and shown in Figure 6 for the Weight (g), the Printing time (sec), the EPC (MJ), and the Compressive strength (MPa) based on the experimental findings presented in the tables above. The results' dispersion on the graphs suggests that a particular control parameter's value has a bigger impact on the related response parameter. As can be observed in Figure 6a, only the LT of 0.1 mm, the PS of 20 mm/s, and the ORA of 45 deg show a scattered distribution of the values for the Printing Time. For the Part Weight (Figure 6b), apart from the ID of 60%, all the other parameters show a scattered distribution of their values. For the Compressive Strength (Figure 6c), all the parameters show a scattered distribution of their values, indicating that all significantly affect how mechanically the components behave when subjected to this specific kind of loading. Only the LT, in particular at 0.30 mm, and the PS, at 40 and 60 mm/s, have compact values for the EPC (Figure 6d), whereas the values of the other control factors are dispersed. In summary, the boxplot presentation of the data showed that it is impossible to draw any firm conclusions about the impact of the control factors and their values on the study's response factors. To determine the influence and relationships between the factors, further information on the experimental data is therefore needed. The study provides such an analysis further below.

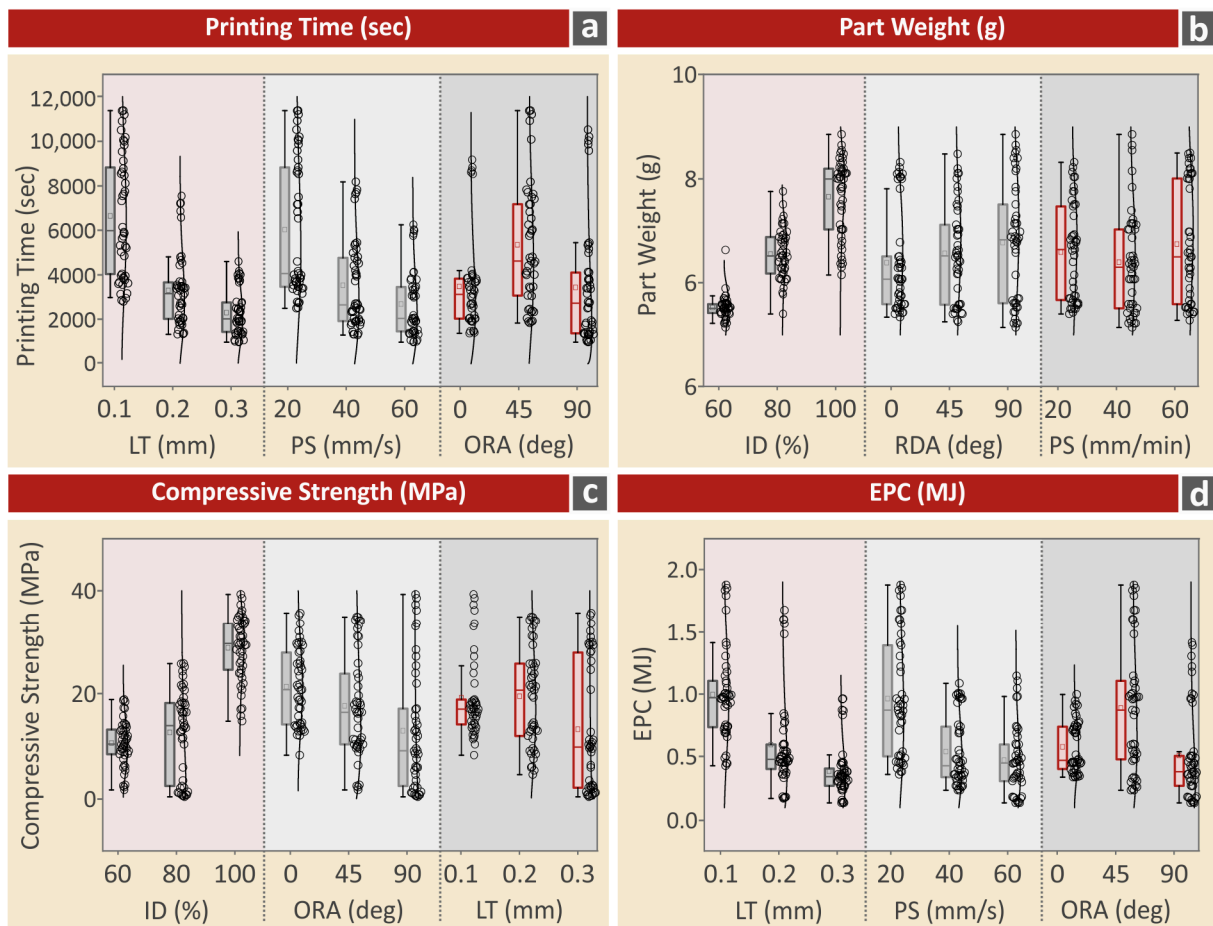


Figure 6. Box plots showing the relationship between the response and the work's control parameters: (a) Printing time vs. PS, LT, ORA; (b) Part weight versus ID, RDA, ORA; (c) Compressive strength versus ID, ORA, RDA; (d) EPC versus PS, LT, ORA.

Main Effect Plots (MEP) were also created using the experimental data shown in the tables above. The MEP are shown in Figures 7 and 8 for the work's most important response parameters. Please refer to the work's supplemental information for extra MEP graphs for the other response factors that were examined in this study (Figures S3 and S4). The

MEP provides details on how each control parameter affects a certain response factor. In addition, the significance of the control parameters for a particular response parameter was graded (from most essential to least important). According to Mostafa et al. [87], the ranking depends on the study of the mean of means and the signal-to-noise ratio. All of the control parameters have a negligible impact on the particular response factor, according to the MEP for the Part Weight (g) (Figure 7), except ID (%), with the increase of it leading to an increase in part weight. The LT and PS control factors have a significant impact on the MEP for the Printing Time (PT), with their rise having the desired effect of causing a decrease in PT. The most important criteria for the PT are LT and PS, which are classified as no. 1 and no. 2, respectively. For the ID, the converse effect occurs: when the ID rises, the PT rises as well. When the ORA factor is between 0° and 90° degrees, reduced PT is given; when the ORA factor is between 45° and 90° degrees, higher PT is reported. NT, RDA, and BT have no considerable impact on PT.

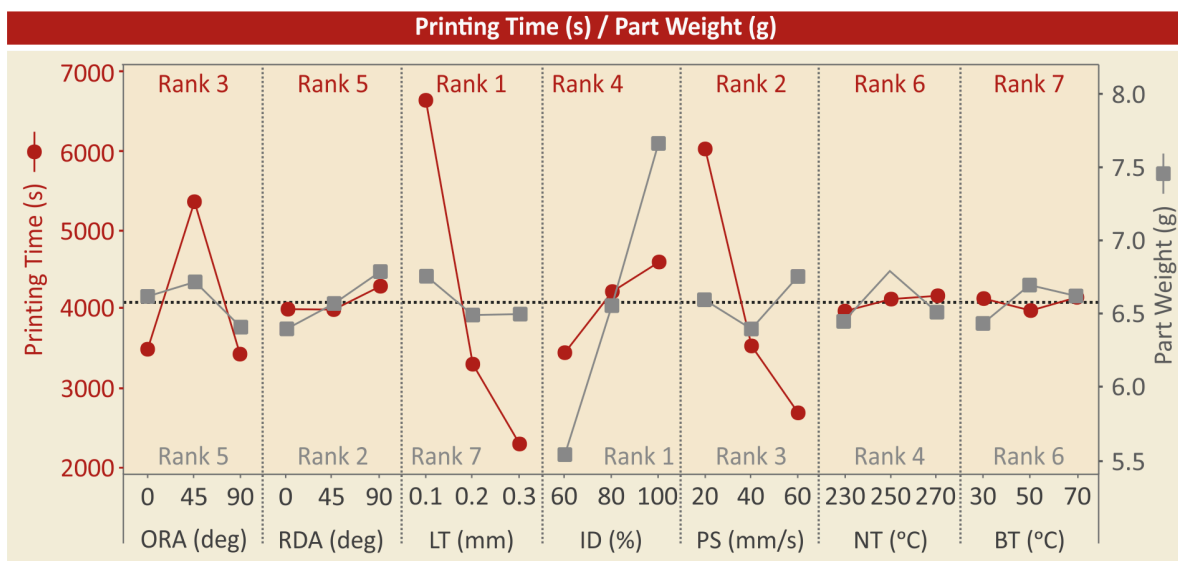


Figure 7. MEP for printing time and part weight versus control settings.

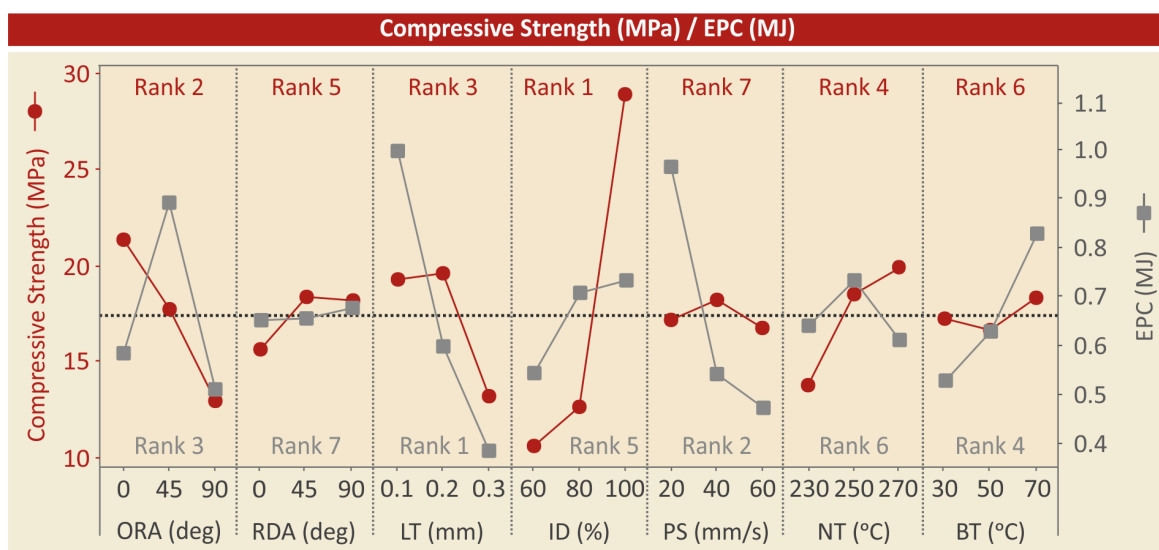


Figure 8. MEP vs. the work's control parameters for compressive strength and energy.

RDA, BT, and PS had no appreciable impact on the Compressive Strength (Figure 8) as a response parameter. The compressive strength is mostly affected by the ID, which is

listed as the top characteristic; as the ID increases, the compressive strength also increases. Compressive strength diminishes as ORA (ranked no2) increases. Furthermore, the highest LT value of 0.3 mm leads to reduced compressive strength values, while lower LT values of 0.1 mm and 0.2 mm produce higher compressive strength values, as shown in Figure 8. The higher compressive strength is achieved with the 0.2 mm LT, which is the median control parameter value still, the difference in compressive strength with the lowest LT value of 0.1 mm is marginal. Also, an increase in compressive strength is caused by an increase in NT.

Higher levels of LT cause a decrease in EPC, making it the dominant parameter in terms of the EPC response factor (ranked no1). Since PS is the second-most important control factor for the EPC, higher PS levels also result in a fall in the EPC. Regarding ORA (ranked as no3), EPC was lower at 0- and 90-degree ORA, while the maximum EPC was recorded at 45 degrees ORA. The EPC is increased by higher BT (ranked fourth) and ID (ranked fifth) values. The EPC is not severely impacted by NT or RDA.

The interaction plots in Figure 9 were created to show the link between the control factors in a graph. Please refer to the work's Supplementary information for extra interaction graphs for the rest of the response factors under consideration (Figure S5). For the EPC:

- The ORA control parameter exhibits synergistic relationships with the LT and PS and antagonistic relationships with the other control parameters.
- The RDA control parameter exhibits a synergistic relationship with the PS and antagonistic relationships with the other control parameters.
- The LT control parameter exhibits a synergistic relationship with the PS, NT, and BT and antagonistic relationships with the other control parameters.
- The ID control parameter exhibits a synergistic relationship with the PS, NT, and BT and antagonistic relationships with the other control parameters.
- The PS control parameter exhibits a synergistic relationship with the ID, LT, and RDA and antagonistic relationships with the other control parameters.
- The NT control parameter exhibits a synergistic relationship with the LT and ID and antagonistic relationships with the other control parameters.
- The BT control parameter exhibits a synergistic relationship with the ID and LT and antagonistic relationships with the other control parameters.
- For compressive strength:
- The ORA control parameter exhibits synergistic relationships with the NT and antagonistic relationships with the other control parameters.
- The RDA control parameter exhibits a synergistic relationship with the NT and antagonistic relationships with the other control parameters.
- The LT control parameter exhibits antagonistic relationships with all the control parameters.
- The ID control parameter exhibits a synergistic relationship with the NT and antagonistic relationships with the other control parameters.
- The PS control parameter exhibits antagonistic relationships with all the control parameters.
- The NT control parameter exhibits a synergistic relationship with the ORA and ID and antagonistic relationships with the other control parameters.
- The BT control parameter exhibits antagonistic relationships with all the control parameters.

Such complex relations between the control parameters indicate that further analysis is required to derive their effect on the response measures studied.

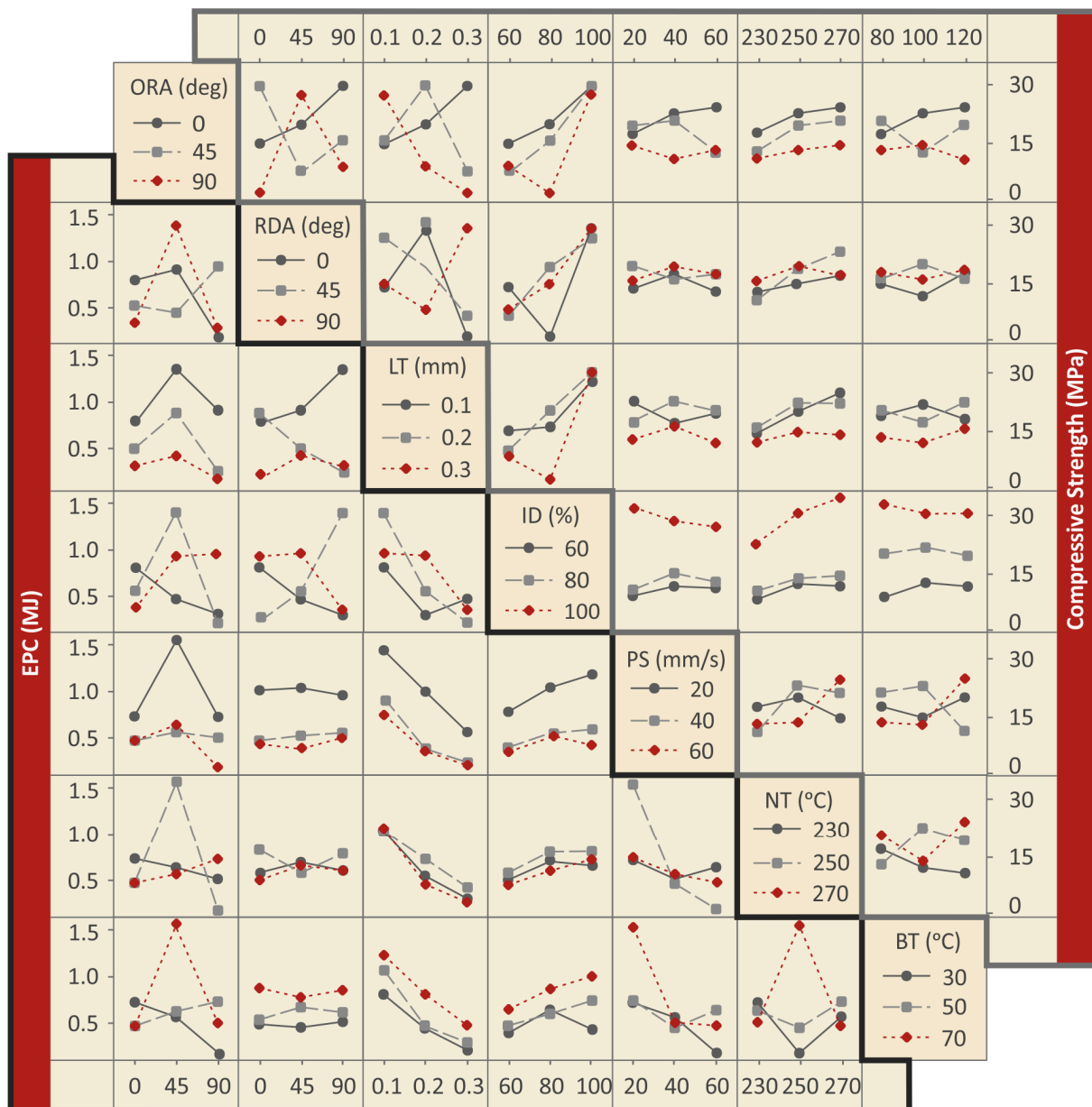


Figure 9. Plots of the compressive strength and the energy in relation to the work’s control factors.

3.3. Regression Analysis

Each response’s Reduced Quadratic Regression Model (RQRM) is computed as follows:

$$Y_k = a_k + \sum_{i=1}^n b_{i,k}x_i + \sum_{i=1}^n c_{i,k}x_i^2 + e_k \tag{6}$$

where k stands for the output quality (for example, printing time, weight, modulus of elasticity, toughness, compressive strength, SPE, SPE, EPC), a, b, c, e, and xi stand for the value that remains persistent, the coefficients of the linear terms, the quadratic terms, the error amount, and the seven control factors, respectively (layer thickness, printing speed, infill density, raster deposition angle, orientation angle, bed, and nozzle temperatures).

The ANOVA for the response measures examined here is shown in tables in the Supplementary material of the work (Tables S3–S10). This investigation resulted in the formation of the related prediction equations for the response factors, which are (7)–(14). It should be noted that in the adjusted mathematical models there are non-significant

parameters, as shown by the collection of *p*-values obtained. It would be interesting to eliminate these non-significant parameters and adjust the models again to avoid over-fitting problems. This was not performed due to the added complexity and length of the work. From the analysis of the ANOVA, the following was derived:

- The F-value for the weight response factor is 45.20 (>4), the *p*-value is almost zero, and the calculated values for the regression parameters are higher than 79.82%. These measures show that the Equation (7) prediction model is adequate for forecasting the weight response factor.
- The F-value for the printing time response factor is 96.61 (>4), the *p*-value is nearly zero, and the calculated values for the regression parameters are higher than 89.69%. These measures show that the Equation (8) prediction model is adequate for forecasting the printing time response factor.
- The F-value for the compressive strength response factor is 67.08 (>4), the P-value is nearly zero, and the calculated values for the regression parameters are higher than 85.66%. These measures show that Equation (9), which serves as the prediction model, is adequate for forecasting the compressive strength response factor.
- The F-value for the compression modulus of elasticity response factor is 43.86 (>4), the *p*-value is nearly zero, and the calculated values for the regression parameters are higher than 79.31%. Based on these metrics, it can be concluded that Equation (10)'s prediction model is adequate for forecasting the compression modulus of the elasticity response factor.
- The F-value for the compression toughness response factor is 59.30 (>4), the *p*-value is nearly zero, and the calculated values for the regression parameters are higher than 84.02%. These measures demonstrate that Equation (11)'s prediction model is adequate for forecasting the compression toughness response factor.
- The EPC response factor's F-value is 168.97 (>4). The regression factor values are computed to be greater than 93.89%, and the *p*-value is almost zero. According to these statistics, the prediction model outlined in Equation (12) is appropriate for predicting the EPC response factor.
- The F-value for the SPE response factor is 233.02 (>4), the *p*-value is nearly zero, and the regression factor values were computed to be larger than 95.51%. These metrics show that Equation (13) in the prediction model is adequate for forecasting the SPE response factor.
- The F-value for the SPP response factor is 34.29 (>4), the *p*-value is nearly zero, and the estimated values for the regression parameter are higher than 74.69%. These measures show that the Equation (14) prediction model is adequate for forecasting the SPP response factor.

$$\begin{aligned}
 \text{Weight} = & -46.1 + 0.00681 \times \text{ORA} + 0.00361 \times \text{RDA} - 6.55 \times \text{LT} + 0.0381 \times \text{ID} - 0.0510 \times \text{PS} \\
 & + 0.3927 \times \text{NT} + 0.0465 \times \text{BT} - 0.000102 \times \text{ORA}^2 + 0.000008 \times \text{RDA}^2 + 13.10 \times \text{LT}^2 \\
 & + 0.000095 \times \text{ID}^2 + 0.000686 \times \text{PS}^2 - 0.000782 \times \text{NT}^2 - 0.000418 \times \text{BT}^2
 \end{aligned} \tag{7}$$

$$\begin{aligned}
 \text{PrintingTime} = & 3301 + 83.88 \times \text{ORA} - 3.20 \times \text{RDA} - 68576 \times \text{LT} + 108.3 \times \text{ID} - 249.7 \times \text{PS} \\
 & + 75 \times \text{NT} - 38.5 \times \text{BT} - 0.9374 \times \text{ORA}^2 + 0.0713 \times \text{RDA}^2 + 117089 \times \text{LT}^2 \\
 & - 0.496 \times \text{ID}^2 + 2.074 \times \text{PS}^2 - 0.140 \times \text{NT}^2 + 0.389 \times \text{BT}^2
 \end{aligned} \tag{8}$$

$$\begin{aligned}
 \text{sB} = & -221 - 0.0701 \times \text{ORA} + 0.0936 \times \text{RDA} + 101.4 \times \text{LT} - 2.369 \times \text{ID} + 0.240 \times \text{PS} + 2.323 \times \text{NT} \\
 & - 0.244 \times \text{BT} - 0.000262 \times \text{ORA}^2 - 0.000717 \times \text{RDA}^2 - 328.7 \times \text{LT}^2 + 0.01766 \times \text{ID}^2 \\
 & - 0.00311 \times \text{PS}^2 - 0.00434 \times \text{NT}^2 + 0.00272 \times \text{BT}^2
 \end{aligned} \tag{9}$$

$$\begin{aligned}
 \text{E} = & -2261 - 3.853 \times \text{ORA} + 0.472 \times \text{RDA} + 678 \times \text{LT} - 12.89 \times \text{ID} + 3.80 \times \text{PS} + 22.61 \times \text{NT} \\
 & - 2.83 \times \text{BT} + 0.02952 \times \text{ORA}^2 - 0.00927 \times \text{RDA}^2 - 2540 \times \text{LT}^2 + 0.1045 \times \text{ID}^2 \\
 & - 0.0497 \times \text{PS}^2 - 0.0445 \times \text{NT}^2 + 0.0266 \times \text{BT}^2
 \end{aligned} \tag{10}$$

$$\begin{aligned} \text{Toughness} = & -26.8 - 0.00006 \times \text{ORA} + 0.01273 \times \text{RDA} + 15.62 \times \text{LT} - 0.3244 \times \text{ID} + 0.0336 \times \text{PS} \\ & + 0.282 \times \text{NT} - 0.0193 \times \text{BT} - 0.000104 \times \text{ORA}^2 - 0.000105 \times \text{RDA}^2 - 49.39 \times \text{LT}^2 \\ & + 0.002393 \times \text{ID}^2 - 0.000401 \times \text{PS}^2 - 0.000517 \times \text{NT}^2 + 0.000251 \times \text{BT}^2 \end{aligned} \quad (11)$$

$$\begin{aligned} \text{EPC} = & -15.35 + 0.014425 \times \text{ORA} - 0.000084 \times \text{RDA} - 6.779 \times \text{LT} + 0.03310 \times \text{ID} - 0.04749 \times \text{PS} \\ & + 0.1320 \times \text{NT} - 0.00464 \times \text{BT} - 0.000169 \times \text{ORA}^2 + 0.000004 \times \text{RDA}^2 + 9.34 \times \text{LT}^2 \\ & - 0.000177 \times \text{ID}^2 + 0.000441 \times \text{PS}^2 - 0.000266 \times \text{NT}^2 + 0.000122 \times \text{BT}^2 \end{aligned} \quad (12)$$

$$\begin{aligned} \text{SPE} = & -1.390 + 0.001746 \times \text{ORA} - 0.000079 \times \text{RDA} - 1.1149 \times \text{LT} + 0.002868 \times \text{ID} - 0.006256 \times \text{PS} \\ & + 0.01347 \times \text{NT} - 0.000936 \times \text{BT} - 0.000021 \times \text{ORA}^2 + 0.000001 \times \text{RDA}^2 \\ & + 1.707 \times \text{LT}^2 - 0.000018 \times \text{ID}^2 + 0.000056 \times \text{PS}^2 - 0.000027 \times \text{NT}^2 \\ & + 0.000020 \times \text{BT}^2 \end{aligned} \quad (13)$$

$$\begin{aligned} \text{SPP} = & 0.146 - 0.000146 \times \text{ORA} + 0.000013 \times \text{RDA} + 0.1033 \times \text{LT} + 0.000355 \times \text{ID} \\ & - 0.000001 \times \text{PS} - 0.001065 \times \text{NT} - 0.000121 \times \text{BT} + 0.000001 \times \text{ORA}^2 - 0.000000 \times \text{RDA}^2 \\ & - 0.2243 \times \text{LT}^2 - 0.000004 \times \text{ID}^2 + 0.000001 \times \text{PS}^2 + 0.000002 \times \text{NT}^2 \\ & + 0.000004 \times \text{BT}^2 \end{aligned} \quad (14)$$

For the response parameters, Pareto plots were created to determine the significant control variables statistically (Pareto charts are provided in the Supplementary part of this study; please see Figures S6–S9).

- The ORA, ORA², LT, LT², PS, and PS² parameters for printing time pass the 1.98 margins, making them statistically significant factors for the particular response factor. The calculated MAPE value of 19.61% is a respectable outcome. Additionally, the Durbin-Watson metric was estimated at 0.4, demonstrating a positive autocorrelation in the prediction residuals.
- ORA², PS, PS², NT, NT², BT, and BT² were the statistically significant characteristics for the part weight. MAPE was computed at 5.05%, which is a highly acceptable result and confirms the model's dependability. The prediction residuals show a positive autocorrelation, according to the 0.96 Durbin-Watson factor calculation.
- The statistically significant parameters for compressive strength include ORA, RDA, RDA², LT, LT², ID, ID², NT, and NT². MAPE was computed at 47.53%, which is a moderate result and shows that the expected accuracy of the model in the prediction is not very good. The residuals of the forecast show a positive autocorrelation, according to the Durbin-Watson factor calculation, which came out to be 1.04.
- The statistically significant factors for the EPC are ORA, ORA², LT, LT², ID, ID², PS, PS², NT, NT², and BT². MAPE was determined to be 15.63%, which is a respectable outcome. The residuals of the forecast show a positive autocorrelation, according to the Durbin-Watson factor calculation, which came up at 0.69.

A three-dimensional surface graph of behavior vs. control factors is shown in Figure 10. The two most important control parameters for each response measure are used to plot the three-dimensional surface graphs, to depict their effect and dependence on the specific measure.

3.4. Confirmation

Two verification runs (28 and 29) were executed to assess the precision of the ANOVA modeling technique. In Run 28, the control parameter values that gave the highest compressive strength results were selected (or values close to them), while in Run 29, the corresponding control parameter values that minimized the EPC were selected. Five replicas of each run were used. Table 4 provides the control variables for these verification runs. Tables 5 and 6 respectively, show the means and variances of the response components for each run (the deviation presented is the calculated one from the experimental results. It refers only to the specific data, so there is no coverage factor). The tables in the work's

Supplementary file contain the experimental results for each replica in the two validation runs, which are displayed analytically (Tables S11 and S12).

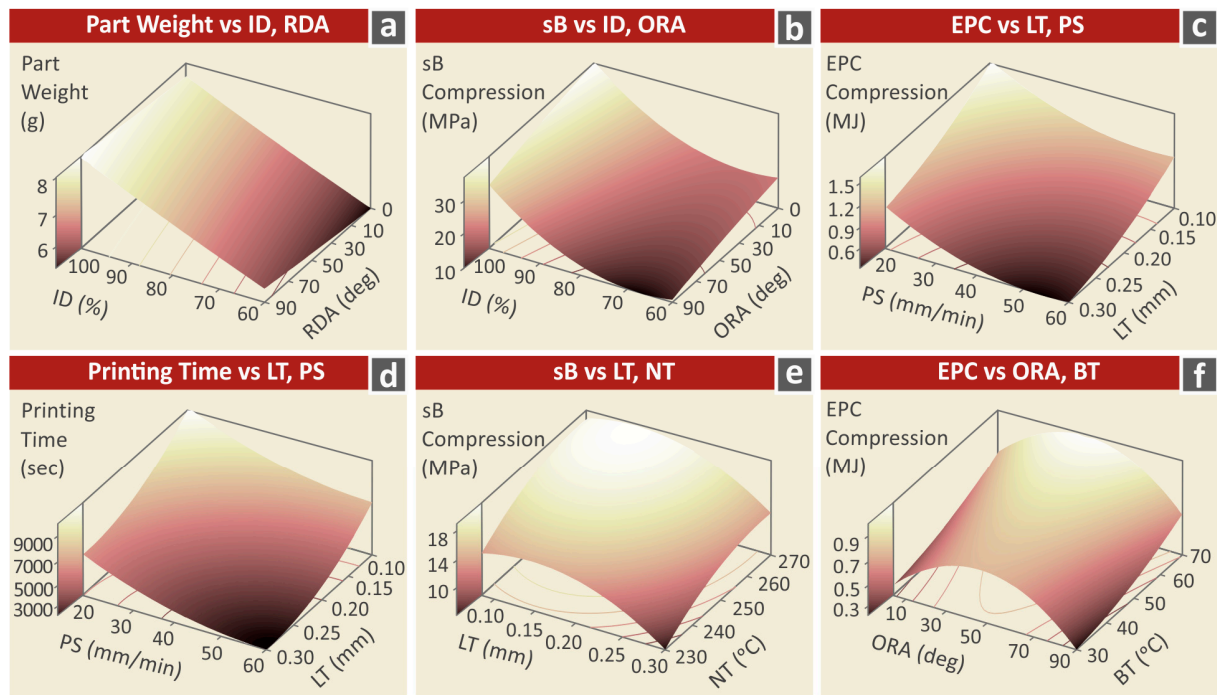


Figure 10. Response versus Control Parameters of (a) Part Weight versus ID and RDA; (b) Compressive Strength versus ID and ORA; (c) Energy versus PS and LT; (d) Printing Time versus LT and PS; (e) Compressive Strength versus LT and NT; (f) Energy versus ORA and BT.

Table 4. Confirmation Runs’ Control Parameters.

Run	ORA	RDA	LT	ID	PS	NT	BT
28	0	65.5	0.15	100	38.6	267.6	70
29	90	10.0	0.30	60	53.9	270.0	30

Table 5. Weight, compressive strength, modulus of elasticity, and toughness mean values and standard deviations of observed responses for the validation runs.

Run	Weight (g)	sB (MPa)	E (MPa)	Toughness (MJ/m ³)
28	7.12 ± 0.19	36.94 ± 1.58	422.58 ± 20.59	5.06 ± 0.19
29	5.32 ± 0.15	3.26 ± 0.55	67.18 ± 3.53	0.56 ± 0.04

Table 6. Printing Time, EPC, SPE, and SPP Measured Responses: Average Values and Standard Deviations for the Confirmation Runs.

Run	Printing Time (s)	EPC (MJ)	SPE (MJ/g)	SPP (kW/g)
28	4745.80 ± 164.74	0.780 ± 0.037	0.120 ± 0.005	0.023 ± 0.001
29	822.80 ± 94.73	0.119 ± 0.009	0.022 ± 0.002	0.028 ± 0.005

For the two confirmation runs, the response factors sB and EPC, predicted vs. actual values, are shown in Table 7, and the difference between these values is calculated. The difference between the two response parameters’ actual and projected values in confirmation run 28 is minimal. The difference between predicted and actual values for sB in confirmation run 29 is negligible. It should be noted that in the specific run (29), the model failed to predict the EPC value, and as a result, the error with the experimental value was

not possible to be calculated (hence the “vague” values in Table 7). In this specific case, the model produced a negative EPC value, which is not physically possible. This shows that the model has restrictions and is expected to produce reliable and accurate results within a specific range of control parameter values. This range was not calculated, as it was not within the scope of the work.

Table 7. Validation Table A.

Run		28	29
Actual	sB (MPa)	36.94	3.26
	EPC (MJ)	0.78	0.12
Predicted	sB (MPa)	41.30	3.56
	EPC (MJ)	0.75	Vague
Absolute Error	sB (%)	11.79	8.95
	EPC (%)	3.97	Vague

4. Discussion

Herein, the effect of seven generic 3D printing settings on the compressive strength and the energy demands for the fabrication of PA6 parts with the MEX method is presented. Experiments were conducted, and the findings were analyzed with statistical modeling. The aim was to locate a set of 3D printing parameters that optimize both the compressive strength and the energy demands for the manufacturing of the corresponding parts. Through the analysis of the results and the modeling process followed it was found that specific 3D printing settings highly affect the performance of the produced parts, and overall, all the 3D printing settings studied contribute to the performance of the parts. For the first time, the compressive strength of PA6 3D printing is studied in such depth (as a function of seven 3D printing settings), revealing once again the importance of selecting proper 3D printing in the MEX process. Additionally, for the first time, according to the authors’ best knowledge, insight into the required energy to 3D print PA6 parts with the MEX method is provided, along with a roadmap on the effect of the 3D printing settings, suggesting the values that achieved more sustainable and eco-friendly results. Sustainability, as mentioned, is a critical parameter nowadays for the AM process. No set of parameters was possible to optimize both the compressive strength and the energy consumption, suggesting that a compromise needed to be made in one or the other direction (mechanical performance or eco-friendliness). Still, specific parameters could achieve more or less good results for both contradictory measures. For example, a 0 deg ORA achieves high compressive strength with reduced energy demands. RDA does not highly affect both measures; the PS and the BT do not significantly affect the compression strength, while their high values significantly reduce the energy demands for the manufacturing of the parts. The NT parameter is not highly affecting the energy demands, while its increase results in higher compressive strength values. The two control parameters that contradict each other are the LT and the ID. High LT values reduce the energy demands but also the compressive strength, while high ID values increase the compressive strength but also the demands.

The ID can affect the compressive strength by almost 300%. This is approximately the difference between the lowest and the highest value recorded by altering only the specific control setting. It should be noted that the literature on the compressive strength of PA6 parts in MEX 3D printing is very limited. Still, the results are in good agreement with the existing literature [88]. The PS, on the other hand, can double the energy demands, with lower PS values requiring twice the energy of the higher values to build the parts (without significantly affecting the compression strength, as mentioned). Such differences justify the need for the analysis carried out in the current work. It should be noted that the EPC values follow the same pattern as the Printing Time values, showing a strong relationship between these two measures. The energy consumption results cannot be directly correlated to the literature since, to the authors’ best knowledge, no study so far has presented corresponding results. Comparing the results presented herein with

corresponding results for the ABS polymer [18], the PA6 polymer requires higher energy amounts to be 3D printed. LT and PS were also dominant parameters in the ABS study regarding energy demands. Similar findings are reported for the PLA [19], the PMMA [21], and the PC [22] polymers, as well. The PMMA required lower energy amounts to be 3D printed, while the PC polymer required significantly higher energy amounts to be 3D printed than the PA6 polymer studied herein.

5. Conclusions

The impact of seven generic, device-independent 3D printing variables on the power usage and mechanical behavior of PA6 items created using the MEX 3D printing technique was thoroughly investigated in this work. Additionally, this is the first time in the literature that, for the specific thermoplastic material (PA6), an optimization of its mechanical properties under compressive loading has been covered in such detail. Finally, it is discussed how the seven 3D printing factors investigated in the study affect two parameters relevant to the overall behavior of the 3D printed samples. The impact of each 3D printing configuration on the parameters that were examined for the energy and mechanical factors was identified as the factors were rated for each response factor analyzed. For each of the response parameters, prediction models were created as functions of the seven control parameters (3D printing settings), and their precision was tested with two validation runs. The precision of the prediction models was confirmed for each of the response characteristics, making them suitable for usage in industrial settings.

In conclusion, it was shown that a single set of 3D printing settings was unable to be utilized to optimize both power consumption and compression strength. Certain response factors can be optimized to meet the requirements of each application, and the predicted models can reveal information about the anticipated outcomes for the remaining response factors. The three main variables were the LT for energy consumption (EPC), the LT for printing time (PT), and the ID for compressive strength (sB). Future research could expand the current study by analyzing control factor values in a new value range, thus extending the range of applications for the findings.

Supplementary Materials: The following supporting information can be downloaded at: <https://www.mdpi.com/article/10.3390/app13158819/s1>, Figure S1. Optical stereoscope image of one randomly selected specimen from each run; Figure S2. Optical stereoscope image of one randomly selected specimen from each run; Figure S3. MEP: SPE (MJ/g) and SPP (kW/g); Figure S4. MEP: Compression modulus of elasticity (Mpa) and Toughness (MJ/m³); Figure S5. Interaction plots: printing time (s), part weight (g); Table S3. Polynomial ANOVA, Weight vs. ORA, RDA, LT, ID, PS, NT, BT; Figure S6. Pareto charts and experimental vs. calculated values graph: (a) printing time (s); (b) part weight (g); Figure S7. Pareto charts and experimental vs. calculated values graph: (a) compressive strength (MPa); (b) EPC (MJ); Figure S8. Pareto charts and experimental vs. calculated values graph: (a) SPE (MJ/g), (b) SPP (kW/g); Figure S9. Pareto charts and experimental vs. calculated values graph: (a) compressive modulus of elasticity (MPa); (b) compressive toughness (MJ/m³); Table S1. Measured Weight, Compressive Strength, Compressive Modulus of Elasticity, and Compressive Toughness for each experimental run and five replicas per run; Table S2. Measured for Printing Time, EPC, SPE, and SPP for each experimental run and five replicas per run; Table S3. Polynomial ANOVA, Weight vs. ORA, RDA, LT, ID, PS, NT, BT; Table S4. Polynomial ANOVA, Printing Time vs. ORA, RDA, LT, ID, PS, NT, BT; Table S5. Polynomial ANOVA, sB vs. ORA, RDA, LT, ID, PS, NT, BT; Table S6. Polynomial ANOVA, E vs. ORA, RDA, LT, ID, PS, NT, BT; Table S7. Polynomial ANOVA, Toughness vs. ORA, RDA, LT, ID, PS, NT, BT; Table S8. Polynomial ANOVA, EPC vs. ORA, RDA, LT, ID, PS, NT, BT; Table S9. Polynomial ANOVA, SPE vs. ORA, RDA, LT, ID, PS, NT, BT; Table S10. Polynomial ANOVA, SPP vs. ORA, RDA, LT, ID, PS, NT, BT; Table S11. Measured Weight, Compressive Strength, Compressive Modulus of Elasticity, and Compressive Toughness for each experimental run and five replicas per run for the Confirmation Runs; Table S12. Measured Printing Time, EPC, SPE, and SPP for each experimental run and five replicas per run for the Confirmation Runs.

Author Contributions: Conceptualization, N.V. and M.P.; methodology, N.V. and M.P.; software, N.M., C.C. and D.S.; validation, N.V., D.S. and E.S.; formal analysis, N.M., C.C. and E.S.; investigation, D.S., N.K.N. and A.M.; resources, N.V. and C.D.; data curation, N.M., C.D. and A.M.; writing—original draft preparation, C.C.; writing—review and editing, M.P.; visualization, N.V.; supervision, N.V.; project administration, M.P.; funding acquisition, N.K.N. All authors have read and agreed to the published version of the manuscript.

Funding: This research received no external funding.

Institutional Review Board Statement: Not applicable.

Informed Consent Statement: Not applicable.

Data Availability Statement: The data presented in this study are available upon request from the corresponding author.

Conflicts of Interest: The authors declare no conflict of interest.

References

1. Newman, S.T.; Zhu, Z.; Dhokia, V.; Shokrani, A. Process Planning for Additive and Subtractive Manufacturing Technologies. *CIRP Ann.* **2015**, *64*, 467–470. [[CrossRef](#)]
2. Peng, T.; Kellens, K.; Tang, R.; Chen, C.; Chen, G. Sustainability of Additive Manufacturing: An Overview on Its Energy Demand and Environmental Impact. *Addit. Manuf.* **2018**, *21*, 694–704. [[CrossRef](#)]
3. MacDonald, E.; Wicker, R. Multiprocess 3D Printing for Increasing Component Functionality. *Science* **2016**, *353*, aaf2093. [[CrossRef](#)] [[PubMed](#)]
4. Javaid, M.; Haleem, A.; Singh, R.P.; Suman, R.; Rab, S. Role of Additive Manufacturing Applications towards Environmental Sustainability. *Adv. Ind. Eng. Polym. Res.* **2021**, *4*, 312–322. [[CrossRef](#)]
5. Mani, M.; Lyons, K.W.; Gupta, S.K. Sustainability Characterization for Additive Manufacturing. *J. Res. Natl. Inst. Stand. Technol.* **2014**, *119*, 419–428. [[CrossRef](#)] [[PubMed](#)]
6. Despeisse, M. The Role of Additive Manufacturing in Improving Resource Efficiency and Sustainability. 2015. Available online: https://link.springer.com/chapter/10.1007/978-3-319-22759-7_15 (accessed on 5 July 2023).
7. Colorado, H.A.; Velásquez, E.I.G.; Monteiro, S.N. Sustainability of Additive Manufacturing: The Circular Economy of Materials and Environmental Perspectives. *J. Mater. Res. Technol.* **2020**, *9*, 8221–8234. [[CrossRef](#)]
8. Niaki, M.K.; Torabi, S.A.; Nonino, F. Why Manufacturers Adopt Additive Manufacturing Technologies: The Role of Sustainability. *J. Clean. Prod.* **2019**, *222*, 381–392. [[CrossRef](#)]
9. Fico, D.; Rizzo, D.; Montagna, F.; Esposito Corcione, C. Fused Filament Fabrication and Computer Numerical Control Milling in Cultural Heritage Conservation. *Materials* **2023**, *16*, 3038. [[CrossRef](#)]
10. Marchewka, J.; Laska, J. Processing of Poly-l-Lactide and Poly(l-Lactide-Co-Trimethylene Carbonate) Blends by Fused Filament Fabrication and Fused Granulate Fabrication Using RepRap 3D Printer. *Int. J. Adv. Manuf. Technol.* **2020**, *106*, 4933–4944. [[CrossRef](#)]
11. Dawood, A.; Marti, B.M.; Sauret-Jackson, V.; Darwood, A. 3D Printing in Dentistry. *Br. Dent. J.* **2015**, *219*, 521–529. [[CrossRef](#)]
12. Shirinbayan, M.; Benfriha, K.; Tcharkhtchi, A. Geometric Accuracy and Mechanical Behavior of PA6 Composite Curved Tubes Fabricated by Fused Filament Fabrication (FFF). *Adv. Eng. Mater.* **2022**, *24*, 2101056. [[CrossRef](#)]
13. Harding, O.J.; Griffiths, C.A.; Rees, A.; Pletsas, D. Methods to Reduce Energy and Polymer Consumption for Fused Filament Fabrication 3D Printing. *Polymers* **2023**, *15*, 1874. [[CrossRef](#)] [[PubMed](#)]
14. Khosravani, M.R.; Reinicke, T. On the Environmental Impacts of 3D Printing Technology. *Appl. Mater. Today* **2020**, *20*, 100689. [[CrossRef](#)]
15. Shuaib, M.; Haleem, A.; Kumar, S.; Javaid, M. Impact of 3D Printing on the Environment: A Literature-Based Study. *Sustain. Oper. Comput.* **2021**, *2*, 57–63. [[CrossRef](#)]
16. Ajay, J.; Rathore, A.S.; Song, C.; Zhou, C.; Xu, W. Don't Forget Your Electricity Bills! An Empirical Study of Characterizing Energy Consumption of 3D Printers. In Proceedings of the 7th ACM SIGOPS Asia-Pacific Workshop on Systems, Hong Kong, China, 4–5 August 2016; Association for Computing Machinery: New York, NY, USA.
17. Annibaldi, V.; Rotilio, M. Energy Consumption Consideration of 3D Printing. In Proceedings of the 2019 II Workshop on Metrology for Industry 4.0 and IoT (MetroInd4.0&IoT), Naples, Italy, 4–6 June 2019; pp. 243–248.
18. Vidakis, N.; Kechagias, J.D.; Petousis, M.; Vakouftsi, F.; Mountakis, N. The Effects of FFF 3D Printing Parameters on Energy Consumption. *Mater. Manuf.* **2022**, *38*, 915–932. [[CrossRef](#)]
19. Vidakis, N.; Petousis, M.; Karapidakis, E.; Mountakis, N.; David, C.; Sagris, D. Energy Consumption versus Strength in MEX 3D Printing of Polylactic Acid. *Adv. Ind. Manuf. Eng.* **2023**, *6*, 100119. [[CrossRef](#)]
20. Petousis, M.; Vidakis, N.; Mountakis, N.; Karapidakis, E.; Moutsopoulou, A. Functionality Versus Sustainability for PLA in MEX 3D Printing: The Impact of Generic Process Control Factors on Flexural Response and Energy Efficiency. *Polymers* **2023**, *15*, 1232. [[CrossRef](#)]

21. Vidakis, N.; Petousis, M.; Mountakis, N.; Moutsopoulou, A.; Karapidakis, E. Energy Consumption vs. Tensile Strength of Poly [Methyl Methacrylate] in Material Extrusion 3D Printing: The Impact of Six Control Settings. *Polymers* **2023**, *15*, 845. [[CrossRef](#)]
22. Vidakis, N.; Petousis, M.; David, C.N.; Sagris, D.; Mountakis, N.; Karapidakis, E. Mechanical Performance over Energy Expenditure in MEX 3D Printing of Polycarbonate: A Multiparametric Optimization with the Aid of Robust Experimental Design. *J. Manuf. Mater. Process* **2023**, *7*, 38. [[CrossRef](#)]
23. Xu, J.; Wang, K.; Sheng, H.; Gao, M.; Zhang, S.; Tan, J. Energy Efficiency Optimization for Ecological 3D Printing Based on Adaptive Multi-Layer Customization. *J. Clean. Prod.* **2020**, *245*, 118826. [[CrossRef](#)]
24. Idrissi, M.A.E.Y.E.; Laaouina, L.; Jeghal, A.; Tairi, H.; Zaki, M. Energy Consumption Prediction for Fused Deposition Modelling 3D Printing Using Machine Learning. *Appl. Syst. Innov.* **2022**, *5*, 86. [[CrossRef](#)]
25. Peng, T.; Sun, W. Energy Modelling for FDM 3D Printing from a Life Cycle Perspective. *Int. J. Manuf. Res.* **2017**, *12*, 83–98. [[CrossRef](#)]
26. Vidakis, N.; Petousis, M.; Velidakis, E.; Liebscher, M.; Mechtcherine, V.; Tzounis, L. On the Strain Rate Sensitivity of Fused Filament Fabrication (FFF) Processed PLA, ABS, PETG, PA6, and PP Thermoplastic Polymers. *Polymers* **2020**, *12*, 2924. [[CrossRef](#)] [[PubMed](#)]
27. Vidakis, N.; Petousis, M.; Mountakis, N.; Maravelakis, E.; Zaoutsos, S.; Kechagias, J.D. Mechanical Response Assessment of Antibacterial PA12/TiO₂ 3D Printed Parts: Parameters Optimization through Artificial Neural Networks Modeling. *Int. J. Adv. Manuf. Technol.* **2022**, *121*, 785–803. [[CrossRef](#)]
28. Kechagias, J.D.; Vidakis, N.; Petousis, M. Parameter Effects and Process Modeling of FFF-TPU Mechanical Response. *Mater. Manuf. Process.* **2021**, *38*, 341–351. [[CrossRef](#)]
29. Petousis, M.; Mountakis, N.; Vidakis, N. Optimization of Hybrid Friction Stir Welding of PMMA: 3D-Printed Parts and Conventional Sheets Welding Efficiency in Single- and Two-Axis Welding Traces. *Int. J. Adv. Manuf. Technol.* **2023**, *127*, 2401–2423. [[CrossRef](#)]
30. Vidakis, N.; David, C.N.; Petousis, M.; Sagris, D.; Mountakis, N. Optimization of Key Quality Indicators in Material Extrusion 3D Printing of Acrylonitrile Butadiene Styrene: The Impact of Critical Process Control Parameters on the Surface Roughness, Dimensional Accuracy, and Porosity. *Mater. Today Commun.* **2022**, *34*, 105171. [[CrossRef](#)]
31. Vidakis, N.; Petousis, M.; Mountakis, N.; Papadakis, V.; Moutsopoulou, A. Mechanical Strength Predictability of Full Factorial, Taguchi, and Box Behnken Designs: Optimization of Thermal Settings and Cellulose Nanofibers Content in PA12 for MEX AM. *J. Mech. Behav. Biomed. Mater.* **2023**, *142*, 105846. [[CrossRef](#)]
32. DePalma, K.; Walluk, M.R.; Murtaugh, A.; Hilton, J.; McConky, S.; Hilton, B. Assessment of 3D Printing Using Fused Deposition Modeling and Selective Laser Sintering for a Circular Economy. *J. Clean. Prod.* **2020**, *264*, 121567. [[CrossRef](#)]
33. Rouf, S.; Raina, A.; Haq, M.I.U.; Naveed, N.; Jeganmohan, S.; Farzana Kichloo, A. 3D Printed Parts and Mechanical Properties: Influencing Parameters, Sustainability Aspects, Global Market Scenario, Challenges and Applications. *Adv. Ind. Eng. Polym. Res.* **2022**, *5*, 143–158. [[CrossRef](#)]
34. Ning, F.; Cong, W.; Qiu, J.; Wei, J.; Wang, S. Additive Manufacturing of Carbon Fiber Reinforced Thermoplastic Composites Using Fused Deposition Modeling. *Compos. B Eng.* **2015**, *80*, 369–378. [[CrossRef](#)]
35. Tanveer, Q.; Mishra, G.; Mishra, S.; Sharma, R. Effect of Infill Pattern and Infill Density on Mechanical Behaviour of FDM 3D Printed Parts- a Current Review. *Mater. Today Proc.* **2022**, *62*, 100–108. [[CrossRef](#)]
36. Christiyan, K.G.J.; Chandrasekhar, U.; Venkateswarlu, K. A Study on the Influence of Process Parameters on the Mechanical Properties of 3D Printed ABS Composite. *IOP Conf. Ser. Mater. Sci. Eng.* **2016**, *114*, 12109. [[CrossRef](#)]
37. Vanaei, H.R.; Raissi, K.; Deligant, M.; Shirinbayan, M.; Fitoussi, J.; Khelladi, S.; Tcharkhtchi, A. Toward the Understanding of Temperature Effect on Bonding Strength, Dimensions and Geometry of 3D-Printed Parts. *J. Mater. Sci.* **2020**, *55*, 14677–14689. [[CrossRef](#)]
38. Chockalingam, K.; Jawahar, N.; Praveen, J. Enhancement of Anisotropic Strength of Fused Deposited ABS Parts by Genetic Algorithm. *Mater. Manuf. Process.* **2016**, *31*, 2001–2010. [[CrossRef](#)]
39. Lee, B.H.; Abdullah, J.; Khan, Z.A. Optimization of Rapid Prototyping Parameters for Production of Flexible ABS Object. *J. Mater. Process Technol.* **2005**, *169*, 54–61. [[CrossRef](#)]
40. Sun, Q.; Rizvi, G.M.; Bellehumeur, C.T.; Gu, P. Effect of Processing Conditions on the Bonding Quality of FDM Polymer Filaments. *Rapid Prototyp. J.* **2008**, *14*, 72–80. [[CrossRef](#)]
41. Anitha, R.; Arunachalam, S.; Radhakrishnan, P. Critical Parameters Influencing the Quality of Prototypes in Fused Deposition Modelling. *J. Mater. Process Technol.* **2001**, *118*, 385–388. [[CrossRef](#)]
42. Yao, T.; Deng, Z.; Zhang, K.; Li, S. A Method to Predict the Ultimate Tensile Strength of 3D Printing Polylactic Acid (PLA) Materials with Different Printing Orientations. *Compos. B Eng.* **2019**, *163*, 393–402. [[CrossRef](#)]
43. Aloyaydi, B.; Sivasankaran, S.; Mustafa, A. Investigation of Infill-Patterns on Mechanical Response of 3D Printed Poly-Lactic-Acid. *Polym. Test.* **2020**, *87*, 106557. [[CrossRef](#)]
44. Somireddy, M.; Czekanski, A.; Singh, C.V. Development of Constitutive Material Model of 3D Printed Structure via FDM. *Mater. Today Commun.* **2018**, *15*, 143–152. [[CrossRef](#)]
45. Ziemian, C.; Sharma, M.; Ziemian, S. Anisotropic Mechanical Properties of ABS Parts Fabricated by Fused Deposition Modelling. In *Mechanical Engineering*; IntechOpen: London, UK, 2012; Volume 2, ISBN 978-953-51-0505-3.

46. Ziemian, S.; Okwara, M.; Ziemian, C.W. Tensile and Fatigue Behavior of Layered Acrylonitrile Butadiene Styrene. *Rapid Prototyp. J.* **2015**, *21*, 270–278. [[CrossRef](#)]
47. Ziemian, C.W.; Ziemian, R.D.; Haile, K.V. Characterization of Stiffness Degradation Caused by Fatigue Damage of Additive Manufactured Parts. *Mater. Des.* **2016**, *109*, 209–218. [[CrossRef](#)]
48. Terekhina, S.; Tarasova, T.; Egorov, S.; Skorniyakov, I.; Guillaumat, L.; Hattali, M.L. The Effect of Build Orientation on Both Flexural Quasi-Static and Fatigue Behaviours of Filament Deposited PA6 Polymer. *Int. J. Fatigue* **2020**, *140*, 105825. [[CrossRef](#)] [[PubMed](#)]
49. Lee, J.; Huang, A. Fatigue Analysis of FDM Materials. *Rapid Prototyp. J.* **2013**, *19*, 291–299. [[CrossRef](#)]
50. Safai, L.; Cuellar, J.S.; Smit, G.; Zadpoor, A.A. A Review of the Fatigue Behavior of 3D Printed Polymers. *Addit. Manuf.* **2019**, *28*, 87–97. [[CrossRef](#)]
51. Casavola, C.; Cazzato, A.; Moramarco, V.; Pappalettera, G. Residual Stress Measurement in Fused Deposition Modelling Parts. *Polym. Test.* **2017**, *58*, 249–255. [[CrossRef](#)]
52. Equbal, A.; Sood, A.K.; Mahapatra, S.S. Prediction of Dimensional Accuracy in Fused Deposition Modelling: A Fuzzy Logic Approach. *Int. J. Product. Qual. Manag.* **2010**, *7*, 22–43. [[CrossRef](#)]
53. Sood, A.K.; Ohdar, R.K.; Mahapatra, S.S. Parametric Appraisal of Mechanical Property of Fused Deposition Modelling Processed Parts. *Mater. Des.* **2010**, *31*, 287–295. [[CrossRef](#)]
54. Terekhina, S.; Skorniyakov, I.; Tarasova, T.; Egorov, S. Effects of the Infill Density on the Mechanical Properties of Nylon Specimens Made by Filament Fused Fabrication. *Technologies* **2019**, *7*, 57. [[CrossRef](#)]
55. Jap, N.S.F.; Pearce, G.M.; Hellier, A.K.; Russell, N.; Parr, W.C.; Walsh, W.R. The Effect of Raster Orientation on the Static and Fatigue Properties of Filament Deposited ABS Polymer. *Int. J. Fatigue* **2019**, *124*, 328–337. [[CrossRef](#)]
56. Luzanin, O.; Plancak, M.; Lužanin, O.; Movrin, D.; Plančak, M. Effect of Layer Thickness, Deposition Angle, and Infill on Maximum Flexural Force in FDM-Built Specimens. *J. Technol. Plast.* **2014**, *39*.
57. McKeen, L.W. 8-Polyamides (Nylons). In *Film Properties of Plastics and Elastomers*, 4th ed.; McKeen, L.W., Ed.; William Andrew Publishing: Norwich, NY, USA, 2017; pp. 187–227. ISBN 978-0-12-813292-0.
58. Jiang, Y.; Loos, K. Enzymatic Synthesis of Biobased Polyesters and Polyamides. *Polymers* **2016**, *8*, 243. [[CrossRef](#)] [[PubMed](#)]
59. Benfriha, K.; Ahmadifar, M.; Shirinbayan, M.; Tcharkhtchi, A. Effect of Process Parameters on Thermal and Mechanical Properties of Polymer-Based Composites Using Fused Filament Fabrication. *Polym. Compos.* **2021**, *42*, 6025–6037. [[CrossRef](#)]
60. Russo, S.; Casazza, E. Ring-Opening Polymerization of Cyclic Amides (Lactams). *Polym. Sci. A Compr. Ref.* **2012**, *4*, 331–396. [[CrossRef](#)]
61. Fang, X.; Simone, C.D.; Vaccaro, E.; Huang, S.J.; Scola, D.A. Ring-Opening Polymerization of ϵ -Caprolactam and ϵ -Caprolactone via Microwave Irradiation. *J. Polym. Sci. A Polym. Chem.* **2002**, *40*, 2264–2275. [[CrossRef](#)]
62. Rwei, S.-P.; Ranganathan, P.; Chiang, W.-Y.; Lee, Y.-H. Synthesis of Low Melting Temperature Aliphatic-Aromatic Copolyamides Derived from Novel Bio-Based Semi Aromatic Monomer. *Polymers* **2018**, *10*, 793. [[CrossRef](#)]
63. Shakeri, Z.; Benfriha, K.; Shirinbayan, M.; Ahmadifar, M.; Tcharkhtchi, A. Mathematical Modeling and Optimization of Fused Filament Fabrication (FFF) Process Parameters for Shape Deviation Control of Polyamide 6 Using Taguchi Method. *Polymers* **2021**, *13*, 3697. [[CrossRef](#)]
64. Singh, R.; Kumar, R.; Ranjan, N.; Penna, R.; Fraternali, F. On the Recyclability of Polyamide for Sustainable Composite Structures in Civil Engineering. *Compos. Struct.* **2018**, *184*, 704–713. [[CrossRef](#)]
65. Azoti, W.L.; Elmarakbi, A. Multiscale Modelling of Graphene Platelets-Based Nanocomposite Materials. *Compos. Struct.* **2017**, *168*, 313–321. [[CrossRef](#)]
66. Spadea, S.; Farina, I.; Carrafiello, A.; Fraternali, F. Recycled Nylon Fibers as Cement Mortar Reinforcement. *Constr. Build. Mater.* **2015**, *80*, 200–209. [[CrossRef](#)]
67. Singh, N.; Hui, D.; Singh, R.; Ahuja, I.P.S.; Feo, L.; Fraternali, F. Recycling of Plastic Solid Waste: A State of Art Review and Future Applications. *Compos. B Eng.* **2017**, *115*, 409–422. [[CrossRef](#)]
68. Ma, Y.; Ueda, M.; Yokozeki, T.; Sugahara, T.; Yang, Y.; Hamada, H. A Comparative Study of the Mechanical Properties and Failure Behavior of Carbon Fiber/Epoxy and Carbon Fiber/Polyamide 6 Unidirectional Composites. *Compos. Struct.* **2017**, *160*, 89–99. [[CrossRef](#)]
69. Ahmadifar, M.; Benfriha, K.; Shirinbayan, M. Thermal, Tensile and Fatigue Behaviors of the PA6, Short Carbon Fiber-Reinforced PA6, and Continuous Glass Fiber-Reinforced PA6 Materials in Fused Filament Fabrication (FFF). *Polymers* **2023**, *15*, 507. [[CrossRef](#)]
70. Mazurkiewicz, M.; Kluczyński, J.; Jasik, K.; Sarzyński, B.; Szachogłuchowicz, I.; Łuszczek, J.; Torzewski, J.; Śnieżek, L.; Grzelak, K.; Małek, M. Bending Strength of Polyamide-Based Composites Obtained during the Fused Filament Fabrication (FFF) Process. *Materials* **2022**, *15*, 5079. [[CrossRef](#)]
71. Hadi, A.; Kadauw, A.; Zeidler, H. The Effect of Printing Temperature and Moisture on Tensile Properties of 3D Printed Glass Fiber Reinforced Nylon 6. *Mater. Today Proc.* **2023**. [[CrossRef](#)]
72. Bhattacharyya, A.R.; Pötschke, P.; Häußler, L.; Fischer, D. Reactive Compatibilization of Melt Mixed PA6/SWNT Composites: Mechanical Properties and Morphology. *Macromol. Chem. Phys.* **2005**, *206*, 2084–2095. [[CrossRef](#)]
73. Dal Conte, U.F.; Villegas, I.F.; Tachon, J. Ultrasonic Plastic Welding of CF/PA6 Composites to Aluminium: Process and Mechanical Performance of Welded Joints. *J. Compos. Mater.* **2019**, *53*, 2607–2621. [[CrossRef](#)]

74. Mahmud, M.B.; Anstey, A.; Shaayegan, V.; Lee, P.C.; Park, C.B. Enhancing the Mechanical Performance of PA6 Based Composites by Altering Their Crystallization and Rheological Behavior via In-Situ Generated PPS Nanofibrils. *Compos. B Eng.* **2020**, *195*, 108067. [[CrossRef](#)]
75. He, Q.; Wang, H.; Fu, K.; Ye, L. 3D Printed Continuous CF/PA6 Composites: Effect of Microscopic Voids on Mechanical Performance. *Compos. Sci. Technol.* **2020**, *191*, 108077. [[CrossRef](#)]
76. Vidakis, N.; Petousis, M.; Tzounis, L.; Maniadi, A.; Velidakis, E.; Mountakis, N.; Kechagias, J.D. Sustainable Additive Manufacturing: Mechanical Response of Polyamide 12 over Multiple Recycling Processes. *Materials* **2021**, *14*, 466. [[CrossRef](#)] [[PubMed](#)]
77. Vidakis, N.; Petousis, M.; Mountakis, N.; Korlos, A.; Papadakis, V.; Moutsopoulou, A. Trilateral Multi-Functional Polyamide 12 Nanocomposites with Binary Inclusions for Medical Grade Material Extrusion 3D Printing: The Effect of Titanium Nitride in Mechanical Reinforcement and Copper/Cuprous Oxide as Antibacterial Agents. *J. Funct. Biomater.* **2022**, *13*, 115. [[CrossRef](#)] [[PubMed](#)]
78. Vidakis, N.; Petousis, M.; Michailidis, N.; Grammatikos, S.; David, C.N.; Mountakis, N.; Argyros, A.; Boura, O. Development and Optimization of Medical-Grade MultiFunctional Polyamide 12-Cuprous Oxide Nanocomposites with Superior Mechanical and Antibacterial Properties for Cost-Effective 3D Printing. *Nanomaterials* **2022**, *12*, 534. [[CrossRef](#)]
79. Petousis, M.; Moutsopoulou, A.; Korlos, A.; Papadakis, V.; Mountakis, N.; Tsikritzis, D.; Ntintakis, I.; Vidakis, N. The Effect of Nano Zirconium Dioxide (ZrO₂)-Optimized Content in Polyamide 12 (PA12) and Polylactic Acid (PLA) Matrices on Their Thermomechanical Response in 3D Printing. *Nanomaterials* **2023**, *13*, 1906. [[CrossRef](#)]
80. Li, Z.; Liu, Y.; Liang, Z.; Liu, Y. The Influence of Fused Deposition Modeling Parameters on the Properties of PA6/PA66 Composite Specimens by the Taguchi Method and Analysis of Variance. *3D Print. Addit. Manuf.* **2023**. [[CrossRef](#)]
81. Farsi, M.; Asefnejad, A.; Baharifar, H. A Hyaluronic Acid/PVA Electrospun Coating on 3D Printed PLA Scaffold for Orthopedic Application. *Prog. Biomater.* **2022**, *11*, 67–77. [[CrossRef](#)] [[PubMed](#)]
82. Vidakis, N.; Petousis, M.; Vairis, A.; Savvakis, K.; Maniadi, A. On the Compressive Behavior of an FDM Steward Platform Part. *J. Comput. Des. Eng.* **2017**, *4*, 339–346. [[CrossRef](#)]
83. Phadke, M.S. *Quality Engineering Using Robust Design*, 1st ed.; Hoboken, N., Ed.; Prentice Hall PTR: Hoboken, NJ, USA, 1995; ISBN 0137451679.
84. Tsu, K.-L. An Overview of Taguchi Method and Newly Developed Statistical Methods for Robust Design. *IIE Trans.* **1992**, *24*, 44–57. [[CrossRef](#)]
85. Antony, J.; Antony, F.J. Teaching the Taguchi Method to Industrial Engineers. *Work. Study* **2001**, *50*, 141–149. [[CrossRef](#)]
86. Vidakis, N.; Petousis, M.; Kechagias, J.D. Parameter Effects and Process Modelling of Polyamide 12 3D-Printed Parts Strength and Toughness. *Mater. Manuf. Process.* **2022**, *37*, 1358–1369. [[CrossRef](#)]
87. Mostafa, K.G.; Montemagno, C.; Qureshi, A.J. Strength to Cost Ratio Analysis of FDM Nylon 12 3D Printed Parts. *Procedia Manuf.* **2018**, *26*, 753–762. [[CrossRef](#)]
88. de Toro, E.V.; Sobrino, J.C.; Martínez, A.M.; Eguía, V.M.; Pérez, J.A. Investigation of a Short Carbon Fibre-Reinforced Polyamide and Comparison of Two Manufacturing Processes: Fused Deposition Modelling (FDM) and Polymer Injection Moulding (PIM). *Materials* **2020**, *13*, 672. [[CrossRef](#)] [[PubMed](#)]

Disclaimer/Publisher’s Note: The statements, opinions and data contained in all publications are solely those of the individual author(s) and contributor(s) and not of MDPI and/or the editor(s). MDPI and/or the editor(s) disclaim responsibility for any injury to people or property resulting from any ideas, methods, instructions or products referred to in the content.